Durham E-Theses

MODELING X-RAY DATA OF BLACK HOLE BINARIES

CHIANG, CHIA-YING

How to cite:

MODELING X-RAY DATA OF BLACK HOLE BINARIES

Chia-Ying Chiang

X-Ray Sub-Group

Extragalactic Astronomy and Cosmology

Department of Physics

University of Durham

Abstract

We test the truncated disc models using multiwavelength (optical/UV/X-ray) data from the 2005 hard state outburst of the black hole SWIFT J1753.5-0127. This system is both fairly bright and has fairly low interstellar absorption, so gives one of the best datasets to study the weak, cool disc emission in this state. We fit these data using models of an X-ray illuminated disc to constrain the inner disc radius throughout the outburst. Close to the peak, the observed soft X-ray component is consistent with being produced by the inner disc, with its intrinsic emission enhanced in temperature and luminosity by reprocessing of hard X-ray illumination in an overlap region between the disc and corona. This disc emission provides the seed photons for Compton scattering to produce the hard X-ray spectrum, and these hard X-rays also illuminate the outer disc, producing the optical emission by reprocessing.

However, towards the end of the outburst, all these conclusions may change. The optical points clearly lie on an extrapolation of the hard X-ray flux, which may indicate that the seed photons for Compton scattering are now self-generated in the flow by Cyclo-Synchrotron radiation rather than being from the disc. The weak soft X-ray emission implies a small disc radius, unchanged from the outburst peak, in conflict with the expectations of the truncated disc model. However, this also requires that the energy to power the corona is advected vertically and radially in a dissipationless fashion from the disc. Thus it seems more likely that the soft X-ray component is not direct emission from the disc itself. We show that a similarly dim low/hard state spectrum from XTE J1118+480 puts similar constraints on the soft X-ray emission region, but here the very low interstellar absorption (an order of magnitude smaller than in SWIFT J1753.5-0127) allows detection of a much larger, cooler, UV component which is well fit by a truncated

disc. Thus whatever the origin of the additional weak soft X-ray emission (irradiation of the inner face as opposed to the top surface of the inner edge of the disc, residual inner disc left from evaporation, ionised reflection, jet etc), its existence as a clearly separate component from the truncated disc in XTE J1118+480 shows that it does not trace the inner disc radius, so cannot be used to constrain the truncated disc models.

Contents

List of Figures

List of Tables

Acknowledgements

First of all I shall offer my heartfelt thanks to my supervisor, Prof. Chris Done. Without her I could never accomplish this thesis. I would like to thank her for accepting me to the program, even though I knew very litter about X-ray astronomy before, and her supervision. I learnt much more than I expected during the past year and it's really pleasant to work with her.

I also want to thank all my friends in Durham. Thank you for accompanying me during the past year. This comforted a girl who was a new comer to a foreign country. I thank people who stayed with me during the Christmas. You made the city no longer a lonely place when everybody went home. I thank my officemates – Jeanette and Jennifer, who solved lots of problems for me. Finally I would like to thank my family and friends in Taiwan. Meanwhile they supported me and kept encouraging me, and I am sure I can not complete my course without their help.

I had a great year in Durham. Thank you all and I will always bear all the happy moments we shared in mind.

Declaration

The work described in this thesis was undertaken between 2008 and 2009 while the author was a research student under the supervision of Professor Christine Done and Dr Timothy Roberts in the Department of Physics at the University of Durham. This work has not been submitted for any other degree at the University of Durham or any other University.

Portions of this work have appeared in the following papers:

- Chiang, C.Y., Done, C., Still, M., and Godet, O., 2009, Monthly Notices of the Royal Astronomical Society (accepted), **An additional soft X-ray component in the dim low/hard state of black hole binaries**

Chapter 1 | *Introduction*

1.1   Black Holes in the Universe

Ever since theoretical models predicted the existence of black holes, they have attracted immense attention. Not only because they are objects with the strongest gravity, but also because they can not be seen. Albert Einstein's Relativity claimed that nothing could exceed speed of light in the vacuum, and a black hole is an object whose escape velocity is even higher than the speed of light. Not even light can escape from a black hole once it crosses the event horizon, which causes the invisibility of these objects. The fact that time and space collapse inside the event horizon evokes speculation by both scientists and novelists.

Dying stars with a central core which is more massive than the Chandrasekhar limit (1.44 $M_\odot$) will collapse into neutron stars; cores more massive than about 3 $M_\odot$ will become black holes. Although astronomers do know the formation stage of stellar-mass black holes, many issues such as black hole spin remain uncertain due to lack of direct observations. In addition, how supermassive black hole form is still unknown, whether their growth is due to mergers (which predicts the emission of yet undetected gravitational waves) or accretion. Thus scientists are still interested in black holes, nearly a century after the models predicted their existence.

The "black" appearance of black holes causes observational difficulties. However,

these darkest objects in the universe are sometimes hidden in some brightest systems, for instance, X-ray binaries (XRBs) and Active Galactic Nuclei (AGN). The black hole itself does not emit light, but when it is accreting material, large amounts of energy can be released via the accretion disc. Therefore, a natural way to study black holes is to study luminous accreting objects. By analyzing the spectra emitted by the accreting material, astronomers then deduce what happens around the black hole. This encourages scientists to study XRBs and AGNs, which harbor stellar-mass black holes and supermassive black holes, respectively. Notwithstanding these two classes of sources differ hugely in mass, they share some similarities. For instance, XRBs and AGNs are both transient sources, but XRBs have much shorter period. The outburst lasts for a few days, and sometimes months or even years for XRBs, but the period could be hundreds of years for AGNs. Because of the convenience of monitoring and possibility of extending study to AGNs, XRBs are popular sources chosen by astronomers to study black holes. This thesis will also focus on the XRB and its accretion flows.

1.2   Accretion Flow: Cool Disc

The structure of accretion flow is decided by the balance between gravitational heating and cooling. Shakura and Sunyaev (1973) developed the standard model of accretion flow around black holes. They found the outward angular momentum transfer of accreting material leads to disc formation around the black hole. Consider a system composed by a rotating accretion disc and a black hole in the center and calculate the energy that the disc can radiate. Assume that the energy released at a given radius is radiated locally, the gravitational potential within a small radius dr can be described as:

$$dE = -\frac{GMm}{r} + \frac{GMm}{r - dr} = \frac{GMm}{r^2}dr, \tag{1.1}$$

where G is the gravitational constant, M is the mass of the black hole, m is the mass of

accreting material, and r is disc radius. Based on Virial Theorem, at most half the energy can be dissipated by viscosity and radiated, and the luminosity at a certain radius should be:

$$dL_{rad} = \frac{GM\dot{m}}{2r^2}dr = dA\sigma T^4 = 2\pi r dr \times 2 \times \sigma T^4. \tag{1.2}$$

The assumption of blackbody radiation will give $T \propto r^{-3/4}$, which means each ring of the disc radiates a blackbody spectrum, whose temperature depends on the distance between the black hole and the ring. Summing these over all radii produces the complete disc spectrum, sometimes described as a multi-color blackbody. The luminosity of closer ring is higher since gravity is stronger, and the area over which this energy is dissipated is smaller so the temperature is higher as well. This solution gives a geometrically thin, optically thick disc unless the mass accretion rate is high enough to generate a luminosity close to the Eddington limit.

1.3   X-ray Transients

A class of sources called X-ray transients (XRTs), which are luminous in the X-ray energy band, accommodate compact objects such as black holes. They spend most of their life in a quiescent state, but the accretion disc goes unstable at the point where Hydrogen goes from being predominantly neutral to ionised. At this point the disc becomes opaque, which causes heating as the energy is trapped in the disc, and then the gas ionises further because of the increasing temperature. The thermal instability triggers the viscous instability, which increases and propagates throughout the accretion disc and finally reaches the inner accretion disc. This gives rise to dramatic, transient outbursts when the luminosity climbs orders of magnitude higher than the original value (e.g. the review by Lasota 2001). The same mechanism also drives Cepheid Variables(CVs), but strong X-ray irradiation is required to explain the outbursts of the XRTs. Many of

these luminous objects are low-mass accreting X-ray binaries (LMXBs) that harbor black holes. The companion star is less massive than the compact object and it transfers matter through its Roche Lobe to the accretion disc, and then the donated mass falls into the black hole, whose mass is typically around 10 solar masses. There are good sources on which to test theories that describe the X-ray spectra of the accretion flow and physical processes happened around strong gravitational fields.

XRTs exhibit two main spectral states – the low/hard state (LHS), and the high/soft state (HSS, alternatively called the thermal dominated state TDS). At low luminosity, the system is in the LHS. At this stage the spectrum is dominated by a hard non-thermal power law component, which comes from the optically thin hot flow filling the interior volume. The hard X-ray emission is attributed to the Comptonisation of the low-energy radiation by the hot corona. Other than hard X-rays, jet activities are detected in radio band in many low-mass accreting X-ray binaries in their LHS (e.g. Fender et al. 2004). This state is also typified by high fractional X-ray variability, often including a distinct low-frequency quasi-periodic oscillation (QPO). As the mass accretion rate reaches a critical value, a transition takes place. The relativistic jet quenches and the thermal emission from the accretion disc dominates the spectrum (see e.g. the review by Done et al. 2007). However, mass accretion rate is not the only parameter which determines the state of an XRT. The hysteresis of the state transition – hard-to-soft state transitions during the rise phase occur at higher luminosities than the soft-to-hard transitions during the decline phase(e.g. Miyamoto et al. 1995; Smith et al. 2002) – indicates that other parameters are also important.

These spectra can be explained by different geometries of the accretion flow. There is a hot, optically thin, geometrically thick solution to the accretion flow equations at low luminosities (Shapiro et al. 1976; Narayan and Yi 1995, see section 1.4). This can be
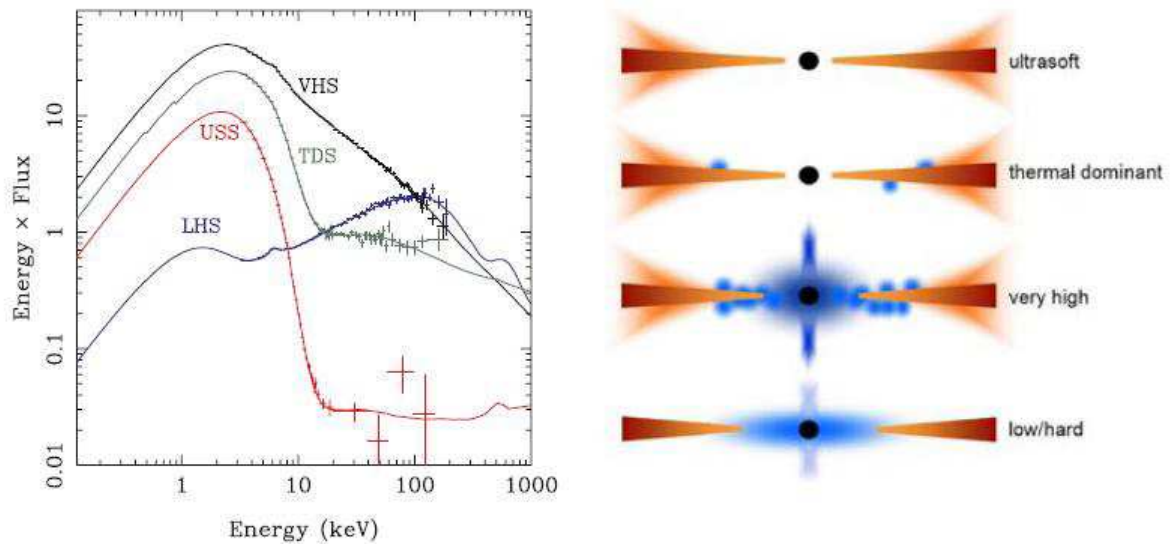
Figure 1.1: The left hand panel shows a selection of states taken from the 2005 outburst of GRO J1655-40. The blue curve shows the spectrum of the system at the low/hard state; the top black curve shows the spectrum at very high state; the grey curve slightly below the black one presents the spectrum of thermal dominant state; the red curve shows the spectrum at ultrasoft state. The right hand panel shows the proposed accretion flow changes to explain these different spectra, with differing contributions from the disc, hot inner flow and its associated jet, active regions above the disc and a wind. (Figure from Done et al. 2007)

put together with a cool, optically thick, geometrically thin disc (Shakura and Sunyaev 1973, see section 1.2) in the truncated disc/hot flow model. The spectral evolution can be explained if the truncated disc progressively replaces more of the inner hot flow as the mass accretion rate increases. This gradually enhances the disc emission while the hard Comptonisation component reduces. The distinct hard/soft spectral transition then marks the point at which the cool disc extends down to the last stable orbit, replacing all the hot flow (Esin et al. 1997; Done et al. 2007), as shown in right panel of Figure 1.1. As a result, the spectrum in the HSS is dominated by the disc emission, which is a combination of multi-color blackbody radiation components.

However, not all the black hole binaries step into the HSS during their outbursts, some systems stay in the hard state in all their outburst epoch, while some go through more than the two main spectral states. The number of spectral states which are seen during the outburst is determined by the peak luminosity. Systems with peak luminosity below $\sim 0.1 L_{Edd}$ remain in the hard state, where the energy output peaks at ~ 100 keV. Brighter systems instead show a distinct transition to the HSS which peaks instead at ~ 1 keV, while the brightest systems can also show a very high state (VHS, alternatively steep power law state, see e.g. the review by Done et al. 2007).

1.4 Accretion Flow: Hotter Solution

Section 1.2 described the disc solution to the accretion flow equations. This gives an explanation to the HSS spectrum, but cannot match the LHS seen at low mass accretion rates. There is obviously a hotter, optical thin component in the LHS that radiates in the form of Comptonisation rather than blackbody emission.

For optical thick flows, energy thermalises due to the multiple electron-photon col-

lisions. At low mass accretion rates, the density drops and electron-photon collisions reduce. Protons probably acquire most of the gravitational energy but these are very inefficient radiators. The observed radiation is caused by electrons, so they must gain energy from the protons. Incomplete thermalisation leads to the formation of a two temperature plasma, where electrons gain energy via Coulomb collisions, and radiate in the form of Comptonisation, bremsstrahlung or cyclo-sychrotron. The proton temperature is close to virial, thus gives the flow a large scale height. Such hot, optically thin, geometrically thick two temperature flows are described by Shapiro et al. (1976).

However, this flow can not be a stable solution without taking proton advection into account. Since the flow is radiatively inefficient, some fraction of the gravitational energy carried by protons goes with them into the black hole. This additional cooling term stabilizes the solution and gives the classic advection-dominated accretion flow(ADAF) model (Narayan and Yi 1995). The truncated disc model combines the theoretical models of a cool, optically thick, geometrically thin disc (section 1.2) at large radii and hot, optically thin, geometrically thick flows described above at small radii. This gives us an alternative solution to the spectrum seen in the LHS.

1.5   Reflection

The emission generated by Comptonization in the corona can irradiate the cooler accretion disc below and cause reflection features (Ross and Fabian 1993). Reflection is set by the balance of photoelectric absorption and Compton scattering. Photoelectric absorption is most efficient at low energies for neutral material, so few photons are reflected. The abrupt increase in absorption at the threshold edge energies of abundant elements cause similar drops in the reflection spectrum (see Figure 1.2(a)). When a photon is absorbed, it knocks an inner-shell electron of the atom out, then the atomic transition takes place
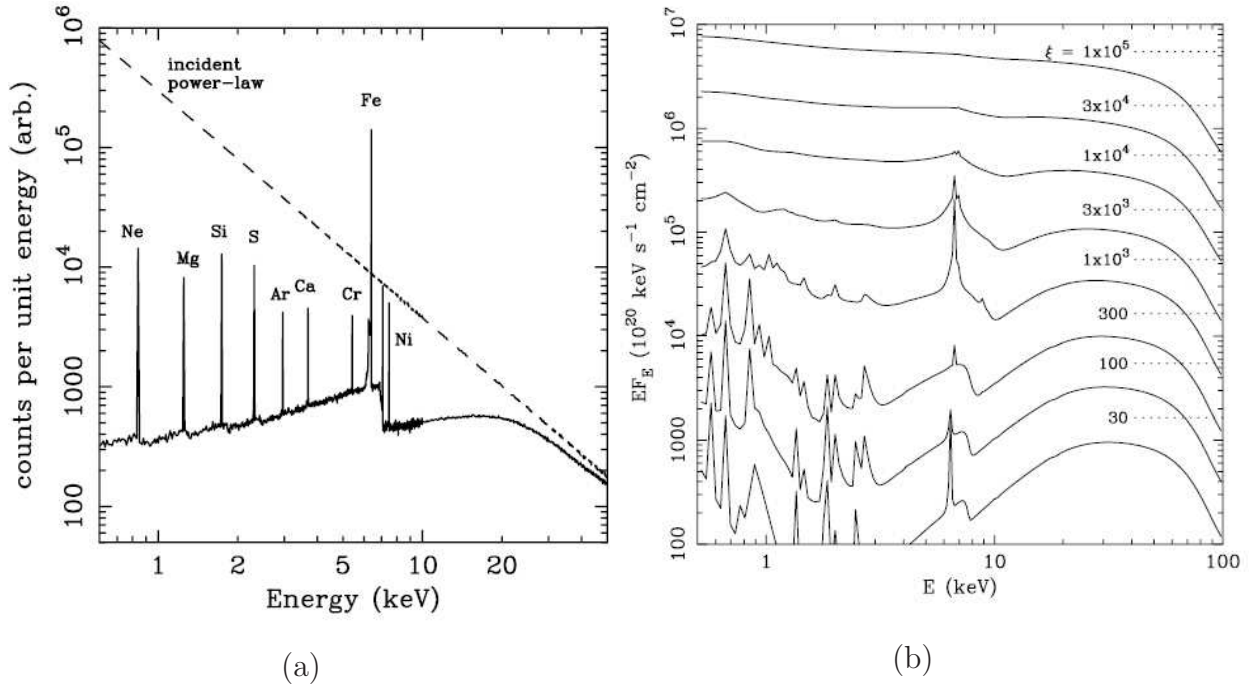
Figure 1.2: Reflection spectra for neutral and ionized material. (a)X-ray reflection from an illuminated slab. Dashed line shows the incident continuum, and solid line shows the reflected spectrum. This is the result of Monte Carlo simulation from Reynolds (1996). (b)Reflection spectra from ionized matter for various values of the ionization parameter ξ ($\xi(r) = 4\pi F(r)/n(r)$, where $F(r)$ is the X-ray flux received per unit area of the disk at a radius r and $n(r)$ is the comoving electron number density. High ξ means highly ionized state). The dotted lines show the level of the illuminating power-law continuum. This figure is from Fabian et al. (2000).
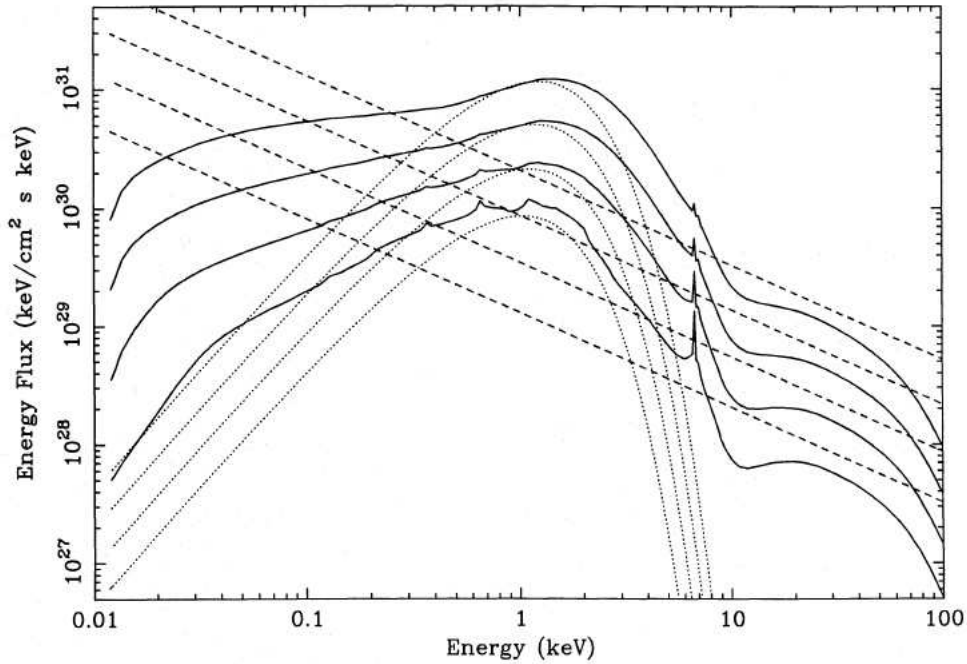
Figure 1.3: Model reflection spectra for the conditions appropriate to a hard power-law flux of photon index 1.8 incident on a section of an accretion disc at 14 R_g around a stellar-mass (10 $M_\odot$) black hole. Accretion rates correspond to fractions $f = 0.15$, 0.20, 0.25 and 0.30 of the Eddington limit. Solid curves show the spectrum entering the surface layer from the disc below, respectively. Fluxes for $f = 0.30$ are correctly shown (top curves of each type); fluxes for $f = 0.25$, 0.20, and 0.15 have been divided by 2, 4 and 8 for clarity of presentation. This figure is from Ross and Fabian (1993).

and emits a photon to make an reprocessing emission line at an energy slightly lower than the threshold of absorption. (see Figure 1.2) Among these emission lines the strongest one is the iron Kα line, which lies at about 6.4 keV, slightly lower than the reflection edge, which is 7.1 keV for neutral iron. At higher energies, photoelectric absorption decreases, reflection rises, but above ~ 50 keV Compton down scattering becomes important, suppressing reflection.

Matt et al. (1993; 1996) found the produced fluorescent line depends upon the ionization state. If the material is weakly ionized, X-ray reflection from the accretion disc produces a cold iron line at 6.4 keV as in neutral material. For intermediate ionized material, Kα line photons are absorbed by ions due to the L shell vacancy and result in a very weak iron line. For highly ionized iron, the energy of both the photoelectric threshold and the Kα line are increased. As the iron is completely ionized, the disc no longer produces reflection features. Reflection spectra from such photoionized material are shown in Figure 1.2(b). The accretion disc of X-ray binary is intrinsically hot so collisional ionization is also important. The simulated reflection spectra are shown in Figure 1.3.

The iron Kα line is intrinsically a narrow line so the line profile is shaped by Doppler and relativistic effects. As shown in Figure 1.4, each radius of the non-relativistic disc generates a double-horned line profile. In the innermost region the orbital velocities are relativistic so causes special relativistic beaming at the blue peak. Gravitational redshifting then moves the line to a lower frequency. Summing the line emission over all radii gives a broadened line profile (see the review of Fabian et al. 2000).

1.6 Motivation

As stated above, if the source is in the HSS, the inner disc is believed to extend to the last stable orbit around the black hole. The spin of black hole determines the position of the last stable orbit. At this stage, there is little emission from Comptonization so the temperature profile of the disc should be set simply by the gravitational field. The maximum disc temperature then gives the innermost disc radius, so a measure of black hole spin. So far, whether black hole spin powers the jet remains unknown, and such models remain untested until black hole spin can be reliably determined. Hence measuring the inner edge of the accretion disc in XRTs is important.
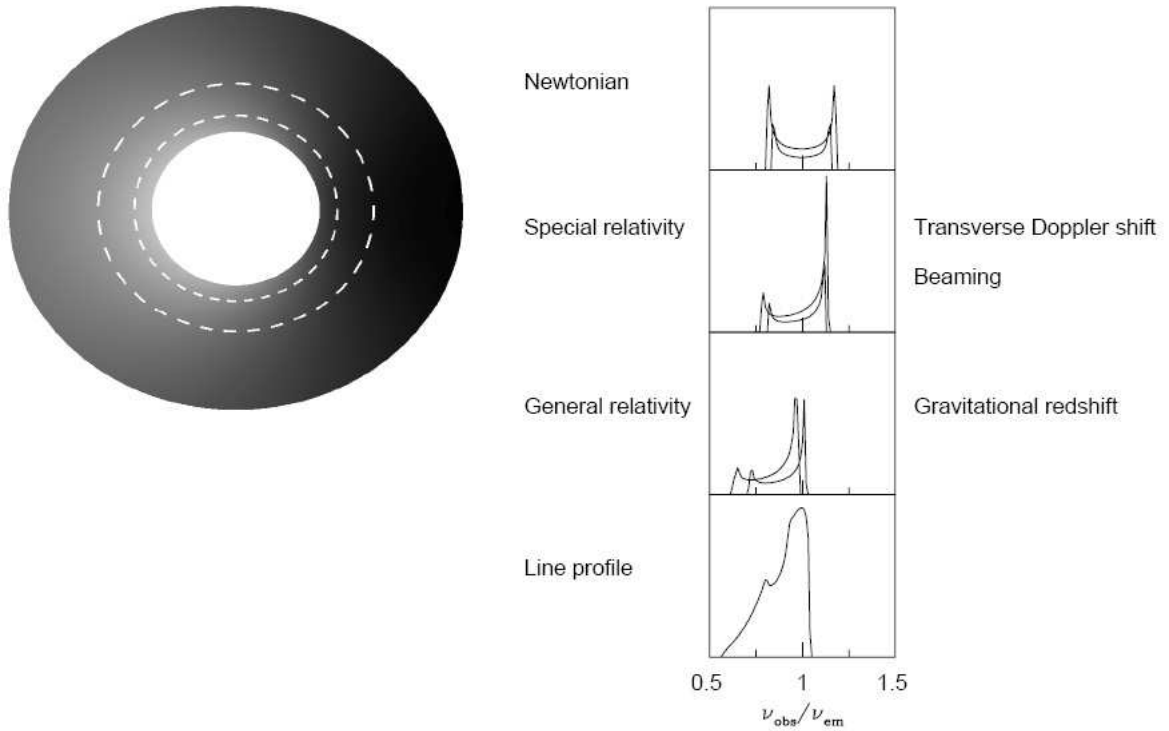
Figure 1.4: The profile of the broad iron line is caused by the interplay of Doppler and transverse Doppler shifts, relativistic beaming and gravitational redshifting. The upper panel shows the symmetric double-peaked profiles from two narrow annuli on a non-relativistic disc. In the second panel the effects of transverse Doppler shifting and relativistic beaming have been included, and in the third panel gravitational redshifting has been included. These totally give rise to a broad, skewed line profile, such as that shown in the lower panel. This figure is from Fabian et al. (2000).

On the other hand, the inner radius of the thin disc in LHS system is also important to constrain because it can be used to test the truncated disc/hot inner flow models described in section 1.2 and 1.4. Based on the ADAF model (see also Figure 1.1 and section 1.4), the inner radius of the cool disc should recede as the LHS drops in luminosity. This can be tested by observations of the temperature and luminosity of the cool disc component. Nevertheless, some observations indicate that the inner disc is not truncated at the hard state (e.g. Miller et al. 2006). Detection of an iron line hugely broadened by the rotating disc at the LHS also suggests the inner radius may be close to the last stable orbit.

Such controversy is caused due to the fact that the disc is not the dominant spectral component in the hard state. Instead, the hard X-ray emission dominates the spectrum except at energies close to the disc maximum temperature. This is rather low at low luminosities, ~ 0.3 keV for a $10M_{\odot}$ black hole at $0.02L_{Edd}$, even if the disc extends down to $6R_g$ (where $R_g = GM/c^2$). Such low energy X-rays cannot be seen with the 3 keV bandpass limit of Rossi X-ray Timing Explorer ($RXTE$), the satellite which has accumulated the most black hole binary (BHB) data to date (Done and Gierliński 2003). Even with CCD detectors which go down to ~ 0.3 keV this component is still not easy to study since low energy X-rays are absorbed by interstellar gas. Most BHBs are in the galactic plane so have gas columns of $N_H \geq 10^{22}$ cm^{-2} which effectively block all emission below 1 keV. All these difficulties mean there are few systems which are suitable for this research. Here we describe one of the best – SWIFT J1753.5-0127.

1.7 Methods to Measure Inner Radius

There are two methods to measure inner radius of the accretion disc for systems in the LHS. The first way is to use the direct disc emission. Equation (1.2) shows that the

maximum disc luminosity should be:

$$L_d = \frac{GM\dot{m}}{2R_{in}}.$$ (1.3)

Similarly, the maximum disc temperature is:

$$T_{max}^4 = \frac{GM\dot{m}}{8\pi\sigma R_{in}^3},$$ (1.4)

so

$$L_d = 4\pi\sigma R_{in}^2 T_{max}^4.$$ (1.5)

There are several corrections factors to go from this very simple derivation to estimate black hole spin. Firstly, conservation of angular momentum leads to a zero stress boundary condition on the last stable orbit. Secondly, the emission from each annulus is not a true blackbody, but can be approximated by a colour temperature correction factor. And the total spectrum is distributed by special and general relativistic effects. However, all these effects can be estimated (Kubota et al. 2001; Done and Gierliński 2003; Done and Davis 2008). Additionally, we need to know the mass of the black hole, distance of the system and the inclination angle. A further limitation is the galactic absorption column of the system needs to be low so that disc emission could be seen before it is completely blocked by interstellar medium.

The alternative way to measure inner radius is by observing the fluorescent iron line. As described in section 1.5, there are some reflection features in the spectra of the LHS. The rotating accretion disc distorts the line-width because of relativistic effects and Doppler effect. By measuring the broadening of the iron line we can estimate the radius at which this orbits. The major advantage of this method is that the reflection features are independent of black hole mass and distance. The iron K-α line also lies at higher energy than disc emission and is less likely to be absorbed by galactic gas. However, these reflection features are generally weak in the LHS, making them difficult to constrain.

In this thesis the first way will be used. Reis, Fabian, Ross and Miller (2009) used the reflection model and obtained a best-fitting $R_{in} = 3R_g$ of SWIFT J1753.5-0127. In 2008, many optical studies of SWIFT J1753.5-0127 came out (see section 1.8) and hence gave measurements of mass and distance, which allow us to revisit the issue via direct disc emission. Thus these data also allow us to compare these methods of deriving R_{in}.

1.8 SWIFT J1753.5-0127

SWIFT J1753.5-0127 was first discovered in the hard X-rays by the Burst Alert Telescope(BAT) on the *Swift* satellite on 2005 May 30 (Palmer et al. 2005). The light curve peaked around early July of 2005 and the total outburst epoch lasted about three months. So far, only one outburst has been detected. The outburst was followed in soft X-rays with the *Swift* X-ray Telescope (XRT) (Morris et al. 2005), in UV with the UV/Optical Telescope (UVOT) (Still et al. 2005), and in radio at a flux density of 2.1 mJy at 1.7 GHz with the Multi-Element Radio-Linked Interferometer Network (MERLIN) (Fender et al. 2005). Optical spectroscopy suggested SWIFT J1753.5-0127 is a X-ray binary system with a low-mass companion star. Cadolle Bel et al. (2005) proposed that SWIFT J1753.5-0127 is a black hole candidate (BHC), as its hard power-law spectrum and 0.6 Hz QPO detected with *RXTE* are characteristic of BHCs at the LHS (Morgan et al. 2005; Ramadevi and Seetha 2007). There is yet no dynamical confirmation of its nature, but it is usually assumed SWIFT J1753.5-0127 is a BHB rather than a neutron star binary (NSB). Light curves of NSBs in hard spectral states generally show X-ray bursts. We examine the light curve of SWIFT J1753.5-0127 and find it is clean and stable in the whole outburst epoch, so we treat it as a BHB.

The orbital period was measured by Zurita et al. (2008), and their best determination is 3.2443 ± 0.0010 hr, which means that SWIFT J1753.5-0127 is the BHC with the

shortest orbital period observed to date. Zurita et al. (2008) also suggested a M2 type or later main-sequence star is required to fit the Roche lobe of a 3.24 hr period orbit. They further estimated the mass and the distance of this source by the difference between orbital period and superhump period. We use their estimation of $M = 12\ M_\odot$ and $d = 5.4$ kpc throughout this thesis. Since the secondary star has not been seen, these results are highly uncertain. Reis, Fabian, Ross and Miller (2009) inferred the spin parameter of this system to be $0.76^{+0.11}_{-0.15}$ and the inclination angle to be $55°^{+2}_{-7}$, by adopting a new reflection model (see Reis et al. 2008).

Public light curves and hardness curves from the *RXTE* All-sky Monitor and pointed observations indicate that SWIFT J1753.5-0127 remained in the hard state throughout its outburst. This was later confirmed by Cadolle Bel et al. (2007) and Zhang et al. (2007). A source like this can be used to study the inner radius in the hard state. Moreover, SWIFT J1753.5-0127 has relatively low absorption columns. There are only a few black holes which have intrinsically low columns which have been observed with CCD detectors, namely XTE J1118+480: $N_H \sim 1.1 \times 10^{20}$ cm^{-2}, XTE J1817-330: 1.1×10^{21} cm^{-2} and SWIFT1753.5-0127: $2 - 3 \times 10^{21}$ cm^{-2} (Cabanac et al. 2009). XTE J1118+480 has only snapshot spectra available (Hynes et al. 2000; Esin et al. 2001; Frontera et al. 2001; 2003), but both SWIFT1753.5-0127 and XTE J1817-330 were well sampled throughout their outbursts by the *Swift* satellite. However, XTE J1817-330 is a long period system, so spends most of its time in the disc dominated state, with only two, rather faint, LHS spectra at the end of its outburst. Thus the short period LHS outburst of SWIFT1753.5-0127 is the best candidate to study the disc evolution in the LHS.

Chapter 2

Data Reduction

2.1 *Swift* Satellite

Swift is part of NASA's medium explorer (MIDEX) program and was launched into a low-Earth orbit on a Delta II 7320-10C rocket on November 20, 2004, and reached a near-perfect orbit of 586×601 km altitude with an inclination of $20°$. This satellite was developed by an international consortium from the United States, United Kingdom, and Italy and aims for a 6-year mission in space. *Swift* is a multi-wavelength space-based observatory dedicated to the study of gamma-ray burst (GRB) science. Its three instruments (BAT, XRT, and UVOT) work together to observe GRBs and their afterglows in the gamma-ray, X-ray, and ultraviolet/optical wavebands, respectively. Based on continuous scans of the area of the sky which one of the instruments monitors, *Swift* uses *momentum wheels* to autonomously quickly slew to the direction of possible GRBs, hence it was named after the agile bird. The XRT and UVOT have co-aligned fields-of-view, both within the BAT field-of-view, so that any source can be observed in all three wavebands.

All discoveries by *Swift* are sent to the ground within seconds and those data are available to other observatories which join *Swift* in observing the GRBs' afterglow. When a GRB occurs, the BAT is the first instrument to detect it. Within about 10 seconds of the burst trigger, the BAT produces a burst localization, which is transmitted to ground observers. In the mean time, the BAT's position is fed to the *Swift* spacecraft which

17
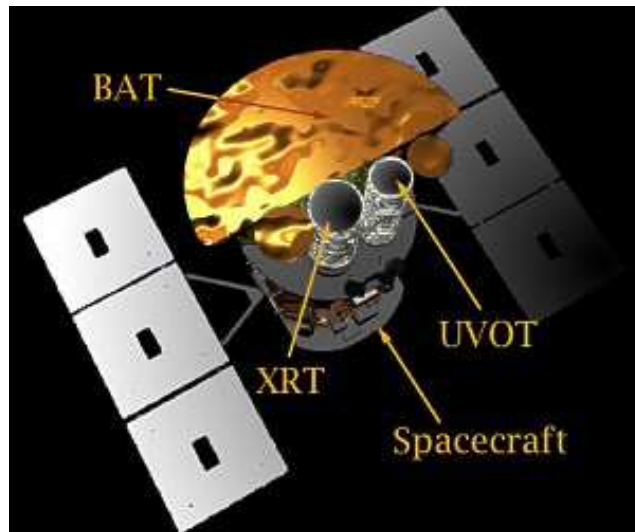
Figure 2.1: *Swift*

brings the GRB into the XRT and UVOT's fields-of-view. In about 60 seconds after a burst trigger, the XRT refines the BAT position. The UVOT can produce an even-more accurate localization within about 200 seconds of the burst trigger. During all of this, the BAT continues observing the GRB to obtain a picture of how the gamma-ray emission evolves over time. In the time between GRB events, *Swift* is available for other science, with open proposal rounds. The data is made available to the world via three different data centers located in the United States (the High Energy Astrophysics Science Archive Research Center, HEASARC), the UK (the UK Swift Science Data Center, UKSSDC), and Italy (the Italian Swift Archive Center, ISAC).

2.1.1 Burst Alert Telescope (BAT)

The BAT is *Swift*'s GRB finder, and its secondary science includes an all-sky hard X-ray survey. It covers a large fraction of the sky and its energy range is 15 - 150 keV.
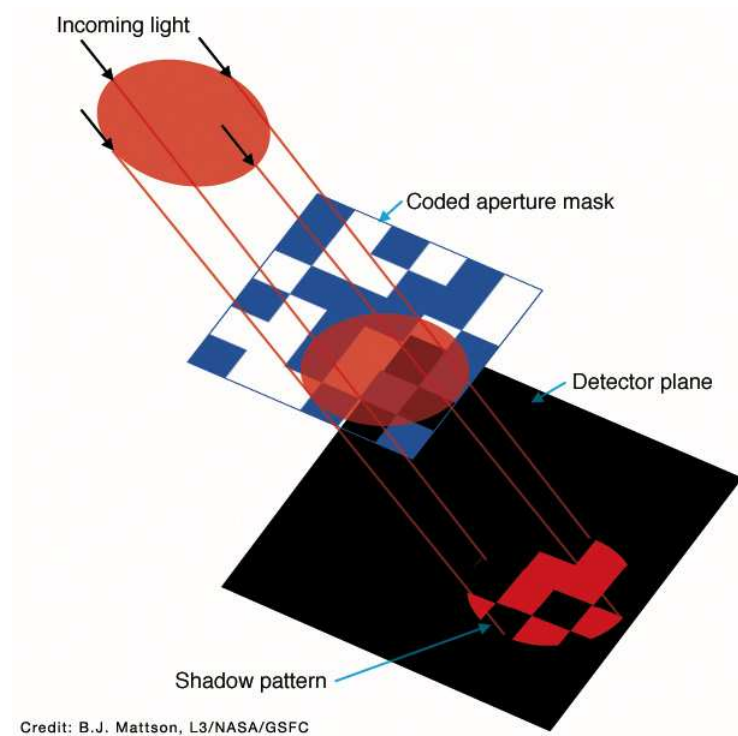
Figure 2.2: coded aperture imaging, from swift.sonoma.edu

The BAT uses a technique called coded aperture imaging to image and localize incoming gamma-rays. A coded aperture is a mask positioned in front of the gamma-ray detectors (see Figure 2.7). As gamma-rays come through the BAT, the lead tiles stop some while the open areas let others through to the detector, so the mask casts a shadow on the detector plane. The computers can then calculate the direction of the gamma-ray source by the position of shadow.

2.1.2   X-ray Telescope (XRT)

Unlike the hard X-rays detected by the BAT, soft X-rays can be focused to produce a direct image. The XRT in this way refines the BAT localization to 5 arcsecond accuracy,

and measures fluxes, spectra, and light curves of GRBs and afterglows. Like other space X-ray telescopes, XRT focuses by "grazing incidence" reflection. These mirrors are nested, one inside another to cover as much area as possible. X-rays coming into the XRT are focused onto a MOS CCD, which was originally designed for the XMM-Newton EPIC MOS cameras. The energy range of XRT is 0.3 - 10 keV.

2.1.3   UV/Optical Telescope (UVOT)

The UVOT further improves the BAT and XRT localizations, giving a position to 0.3 arcsecond accuracy. It is also used to make long term follow-up of afterglow lightcurves. The UVOT is a 30-cm reflecting telescope and was designed on the basis of the Optical Monitor aboard XMM-Newton. The UVOT provides a sub-arcsecond resolution position and provides photometry through lenticular filters in optical and ultra-violet. There are U, B, and V filters, two broadband UV filters centered on 180 and 260 nm, and a narrow UV filter centered on 220 nm on the UVOT.

2.1.4   *Swift* Data Reduction

We use publicly available *Swift* data from SWIFT J1753.5-0127 taken during the period from July 2005 to July 2007. We extracted both X-ray telescope(XRT) and UVOT data for 58 datasets in total. All of our XRT data was in Windowed Timing mode, and we extracted source counts using a circle with radius of 20 pixels. Background was taken from an off source region using a circle of the same size. However, the source was very bright during the peak of the outburst, and some of the datasets were piled up as the count rate was above 100 counts s^{-1}. We determined the size of the central piled up region by excluding progressively larger radii regions until the spectra stopped softening at high energies. This gave an exclusion region of 3 pixels for brightest observations,
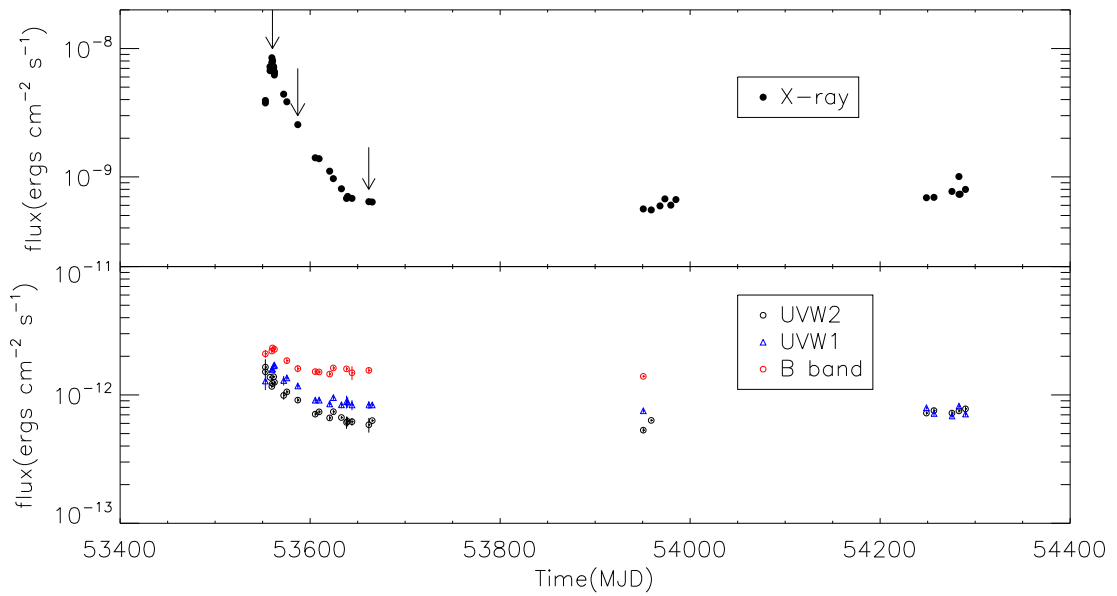
Figure 2.3: The top panel shows the evolution of the observed flux in the *Swift* XRT band, while the lower panel shows the simultaneous UVOT data (in UVW1, UVW2 and B filters, where available). The arrows show the observation time of some representative observations (peak, midway of decline and the end of the outburst from left to right) we pick for further discussion in the later chapter.

and 2 pixels for more moderately piled up data. The effective energy band for XRT is 0.3-10 keV. Nevertheless, there are occasional features seen at 0.4 keV which influenced our fitting results. On the advice of the *Swift* team, we ignore the low energy XRT data, so the effective energy band is 0.5-10 keV.

The flux evolution in the X-ray and UV band is plotted in Figure 2.3, where the upper and lower panels show the X-ray and UV data, respectively. The X-ray flux is calculated by integrating the absorbed model flux of XRT data from 0.5 - 10 keV. For UV data, we define the effective bandpass of each filter to be between the energies determined by its FWHM. The UVOT fluxes are the integrated absorbed model flux within this effective energy band, which is 5.6×10^{-3} to 7.45×10^{-3} keV for UVW2 filter, 4.2×10^{-3} to 5.45×10^{-3} keV for UVW1 filter, and 2.55×10^{-3} to 3.2×10^{-3} keV for B filter. The observations fall into 3 clearly distinct time segments. The first covers the outburst rise and decline, after which the flux then remained fairly constant. Clear instrumental residuals around 1.8 keV (silicon) and 2.2 keV (gold) were found in the second and third data groups, indicatively the response is changing with time. Hence in this thesis we concentrate only on the first data group, in order to track the disc during the flux decline.

2.2 *RXTE* Satellite

The Rossi X-ray Timing Explorer (*RXTE*) was launched from Cape Canaveral on 30 December 1995 on a Delta II rocket that put *RXTE* into its intended low-earth circular orbit at an altitude of 580 km, corresponding to an orbital period of about 90 minutes, with an inclination of 23°. The spacecraft was designed and built by the Engineering Directorate at NASA Goddard Space Flight Center in Greenbelt, Maryland. *RXTE* was designed for a 2-year mission with a goal of five, but now it has well passed the goal and still performs well. *RXTE* is a satellite that observes the time structure of astronom-

ical X-ray sources, such as black holes, neutron stars, X-ray pulsars and X-ray bursts. Time scales from microseconds to months are covered in a spectral range from 2-250 keV. The mission carries two pointed instruments, the Proportional Counter Array (PCA) developed by GSFC to cover the lower part of the energy range, and the High Energy X-ray Timing Experiment (HEXTE) developed by UCSD covering the upper energy range. *RXTE* also carries an All-Sky Monitor (ASM) from MIT. Data from the PCA and ASM are processed on board by the Experiment Data System (EDS), also built by MIT.

The EDS consists of eight Event Analyzers (EA), of which six are dedicated to the PCA and two to the ASM. Each EA contains an Intel 80286 processor and associated memory. The EDS is capable of processing up to 500,000 counts per second, and can time the arrival of individual X-rays to about 1 microsecond. The data can be collected in a number of different data modes simultaneously. This facilitates collection and analysis of the data appropriate to different sources. Data from HEXTE is handled similarly by a separate data system. Observations from *RXTE* have been used as evidence for the existence of the frame-dragging effect predicted by the theory of general relativity. *RXTE* results have, as of mid-2009, been used in more than 1700 scientific papers.

2.2.1 Proportional Counter Array (PCA)

The PCA has five xenon gas proportional counter detectors (the X-rays interact with the electrons in the xenon gas) that are sensitive to X-rays with energies from 2-60 keV. Each proportional counter unit has a net geometric collecting area of $\sim 1600\ cm^2$. The PCA's pointing area overlaps that of the HEXTE instrument. Every event passes information over a serial interface to the EDS. The EDS applies a time-tag and performs event selection and (multiple) data compressions. Two standard compression modes have
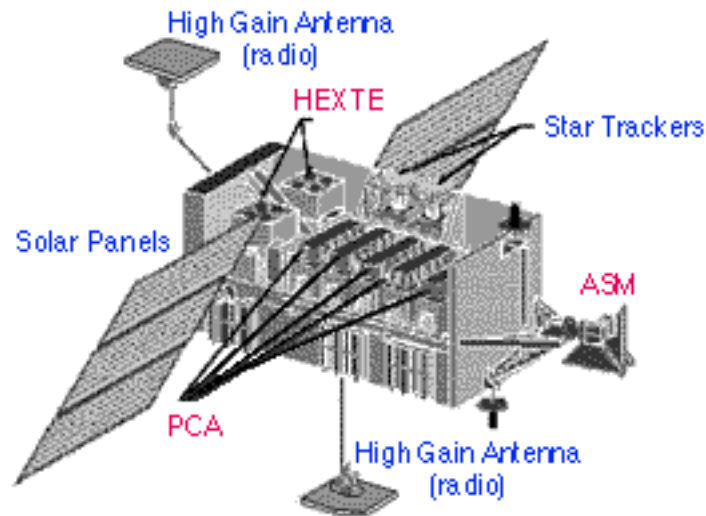
Figure 2.4: *RXTE* satellite, from http://heasarc.gsfc.nasa.gov/docs/xte/learning_center/
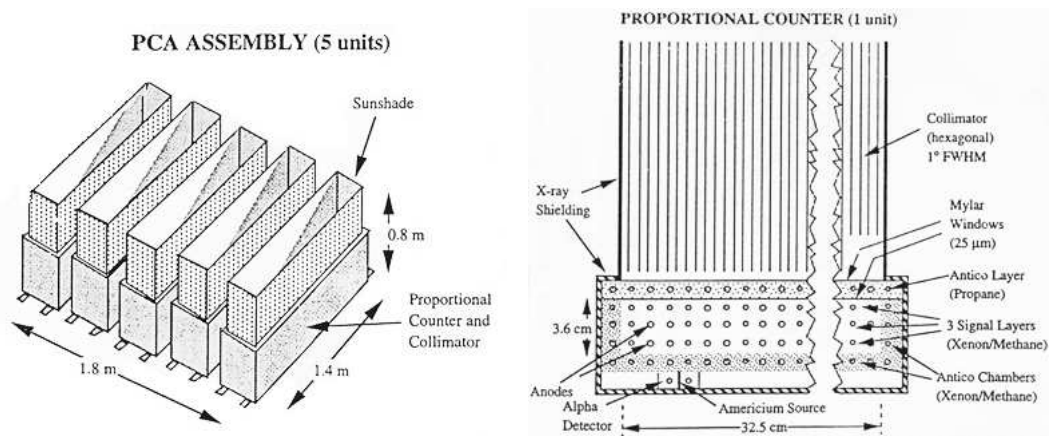
Figure 2.5: PCA and PCU, from http://heasarc.gsfc.nasa.gov/docs/xte/xte_images.html

been run throughout the entire mission. Standard 1 provides light curves with 0.125 sec resolution and calibration spectra with full pulse height information collected every 128 seconds. Standard 2 provides pulse height information for each layer of each detector with 16 second resolution and 29 rates which account for all the "non X-ray" events. Both Standard modes count each event produced by the PCA exactly once.

2.2.2 High Energy X-ray Timing Experiment (HEXTE)

The HEXTE consists of two clusters each containing four phoswich scintillation detectors collimated to a 1° FWHM field of view and co-aligned with the PCA. Each detector has a net open area of $\sim 225\ cm^2$ and covers the energy range 15-250 keV, with an intrinsic spectral resolution better than 9 keV at 60 keV. Each cluster can "rock" along mutually orthogonal directions to provide background measurements 1.5° or 3° on either side of the source. The HEXTE detects each incident X-ray photon individually, and outputs data from these events in flexible formats to provide spectroscopy and timing from $7.6\mu s$ upwards, limited primarily by photon statistics (for faint sources) and the restrictions on the telemetry rate (for bright sources). An X-ray photon interacting with sufficient energy deposition will generate an event which has arrival-time and energy-related parameters associated with it. Like the PCA, the HEXTE is a spectro-photometer, not an imaging instrument, and no position information is obtained from the detectors.

2.2.3 All-Sky Monitor (ASM)

The ASM scans about 80% of the sky every orbit, allowing monitoring at time scales of 90 minutes or longer, at 2-10 keV, monitoring the long-term behavior of a number of the brightest X-ray sources, and giving observers an opportunity to spot any new phenomenon quickly. The ASM consists of three wide-angle shadow cameras equipped with proportional counters with a total collecting area of 90 cm^2. Events detected by the ASM will be processed on board by the EDS before insertion into the telemetry stream.

2.2.4 *RXTE* Data Reduction
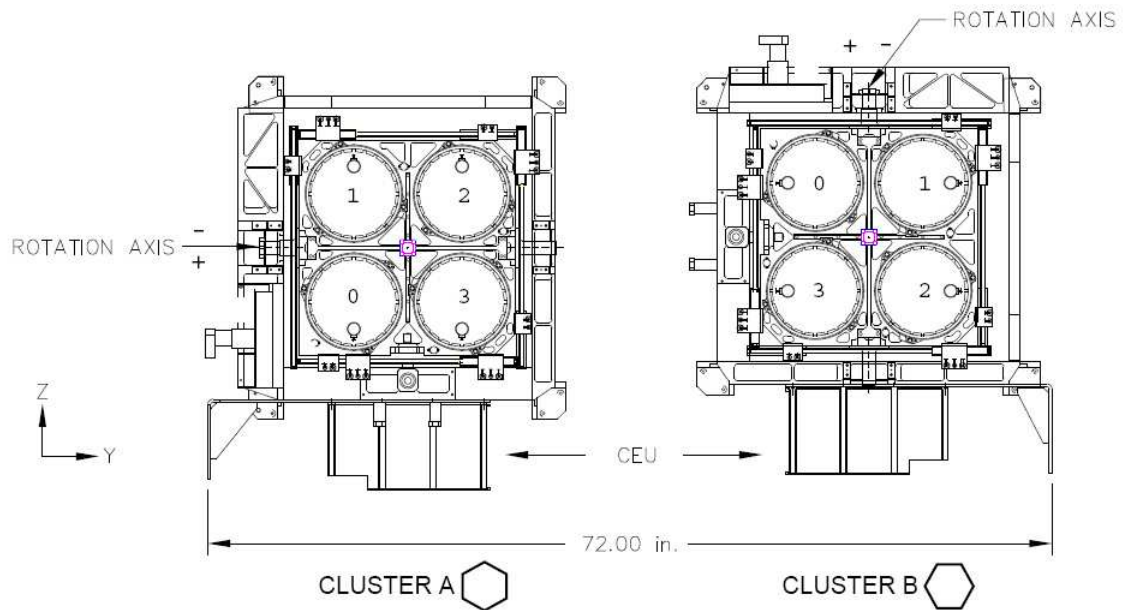
Figure 2.6: HEXTE structure, from

http://mamacass.ucsd.edu:8080/hexte/hexte_docs.html
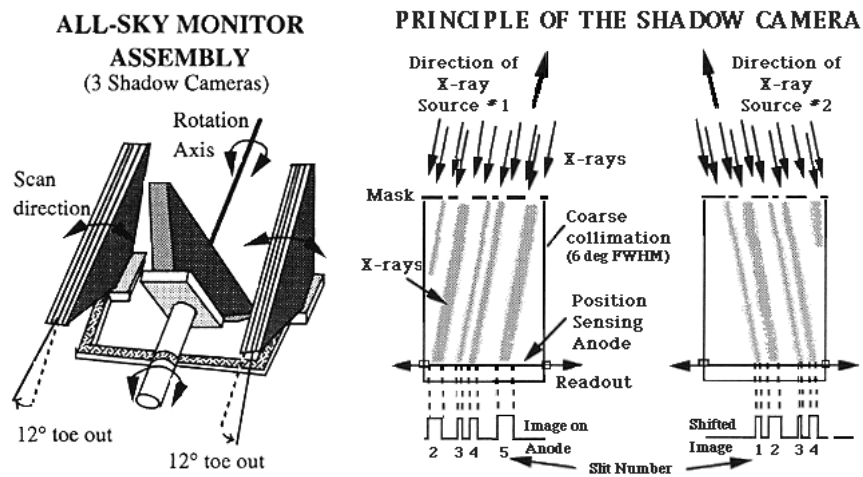
Figure 2.7: ASM and principle of shadow camera, from

http://heasarc.gsfc.nasa.gov/docs/xte/xte_images.html
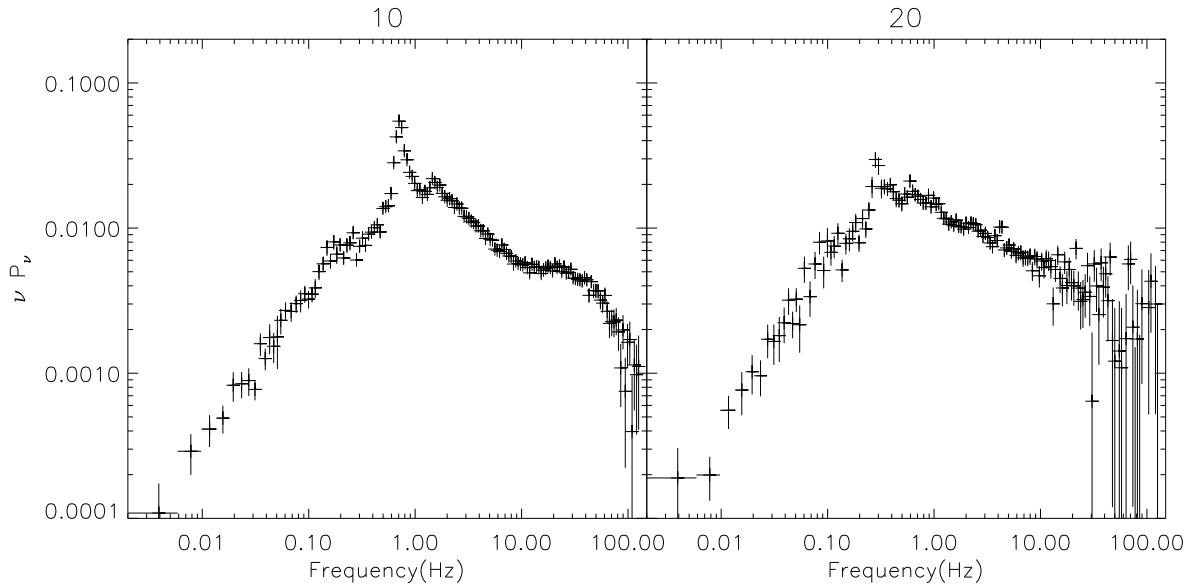
Figure 2.8: This figure shows the power density spectra of the peak (10) and the midway of the outburst decline (20), which is the last dataset in which the QPO is significant. Energy spectra of these observations are shown in Chapter 3. The QPO frequency is clearly visible during at the peak of the outburst. Then it becomes less and less obvious until no longer detectable.

As stated in Chapter 1, the *RXTE* satellite also followed the 2005 outburst. We use the standard extraction techniques with the bright source background to derive PCA spectra from all layers of detector 2, adding 1 percent systematic error and use these data from 3-16 keV. Data retrieved by HEXTE in cluster 0 are also used over the energy range 25-200 keV. We also do timing analysis on *RXTE* data and obtain the power density spectra (PDS, Figure 2.8 shows PDS in the peak and midway through the outburst decline) of the PCA lightcurves. By fitting the PDS with Lorentzians, the quasi-periodic oscillation (QPO) frequency can be found. Table 2.1 shows this for the first 10 observations in which the QPO is detected.

Number	*RXTE* observation ID	MJD	QPO frequency(Hz)
00	91094-01-01-00	53553.04	0.64 ± 0.01
04	91423-01-01-04	53557.22	0.91 ± 0.01
03	91094-01-01-04	53557.48	0.83 ± 0.01
07	91094-01-02-01	53559.71	$0.75^{+0.01}_{-0.02}$
10	91094-01-02-00	53560.49	$0.72^{+0.00}_{-0.01}$
13	91094-01-02-02	53561.48	0.70 ± 0.01
16	91094-01-02-03	53562.59	0.63 ± 0.01
18	91423-01-03-06	53572.88	0.47 ± 0.01
19	91423-01-04-02	53575.50	$0.45^{+0.00}_{-0.01}$
20	91423-01-06-00	53587.63	0.29 ± 0.01

Table 2.1: We process our *RXTE* data to obtain power density spectra (PDS) and fit the PDS with Lorentzian function. The QPO frequency varies from ~ 0.3 Hz to ~ 0.9 Hz.

We select the subset of *Swift* and *RXTE* data which are taken within one day of each other. This gives a total of 27 observations which have quasi-simultaneous coverage of the optical/UV/X-ray/hard X-ray spectrum. The *Swift* and *RXTE* data complement each other very well as *Swift* data does not have as good signal-to-noise ratio as *RXTE*. Nevertheless, *RXTE* does not cover the bandpass below 3 keV as *Swift* does (for details see section 2.1.2), and this makes the disc emissions in the LHS undetectable in *RXTE* even for sources with low N_H. The soft X-rays taken by the XRT and UV/optical emission retrieved by the UVOT give us chance to constrain the disc properties. *RXTE* data, on the other hand, gives a much better constraint on the high energy spectra, and hence the bolometric luminosity.

Chapter 3

Spectral Fitting and Results

Our combination of *Swift* and *RXTE* data gives us spectra spanning optical/UV/soft and hard X-rays accross the whole outburst of SWIFT J1753.5-0127. We now use these to track the evolution of the accretion disc.

3.1 Simple Model

We first concentrate on the X-ray data alone. Since the source remained in the hard state, we model this using a disc and thermal Comptonisation, where the seed photons for the Compton scattering are assumed to be from the disc. Because we use *RXTE* data as well, the reflected continuum should be included. Our model includes the self-consistent iron line from the disc assuming that the material is neutral, with solar abundances and inclined at 60° (Zycki et al. 1999). We fix the galactic absorption column at $N_H = 0.2 \times 10^{22}$ cm^{-2} corresponding to an $E(B - V) = 0.34$ (Cadolle Bel et al. 2007). The results for each spectrum are detailed in Table 3.1. We assess the significance of the detected disc emission by removing the disc from the model, and fixing the seed photon temperature instead at 0.1 eV. This results in a loss of 2 degrees of freedom, so the disc is only significant at greater than 99 per cent confidence for $\Delta\chi^2 > 4.61$. Thus all the spectra apart from the final 3 (26, 30 and 31) strongly require the presence of an additional soft component as well as a single power law and its reflection.

Figure 3.1 shows the derived disc temperature and radius(see Table 3.1). The disc radius *decreases* as the outburst progresses (see also Cabanac et al. 2009), in apparent conflict with the truncated disc model where the inner disc should progressively increase during the LHS decline. Yet the amount of reflection from the disc decreases, as expected from the truncated disc models.

3.2 Optical data

We show these X-ray model fits extrapolated down to the optical/UV data and corrected for the effects of interstellar absorption. Figure 3.2a shows this for the outburst peak (10). This clearly shows that extrapolating the hard X-ray power law spectrum down in energy *overpredicts* the optical/UV data. This implies that the hard X-ray spectrum must break at UV/soft X-ray energies, supporting our modelling of it as due to Comptonisation of seed photons from the accretion disc. However, extrapolating the soft X-ray disc emission *underpredicts* this emission, making it clear that intrinsic gravitational energy release in the disc is insufficient to produce the observed optical/UV data.

In general, the optical can include additional contributions from reprocessed emission from hard X-ray illumination of the outer disc, as well as contributions from the jet and the companion star (e.g. Russell et al. 2006). However, SWIFT J1753.5-0127 is a short period, low mass X-ray binary, so the companion star must faint. Instead we try to quantify the jet contribution from observed radio flux of ~ 2.1 Jy at 1.7 GHz (Fender et al. 2005. We show the extrapolation of this up through our optical/UV/X-ray bandpass assuming a flat spectrum (black line on Figure 3.2a). This is a factor ~ 3 below the observed optical flux, but this is the maximum possible jet contribution as its spectrum should break where it becomes optically thin. It seems most likely that this break is at IR frequencies (Markoff et al. 2001; Gallo et al. 2007) so the jet is also probably negligible

Number	Swift	RXTE	$kT_{disc}(keV)$	N_{dbb}	Γ	$\Omega/2\pi$	N_{pl}	χ^2/ν	$\triangle\chi^2$
00	00143778000	91094-01-01-00	0.22 ± 0.01	47557	1.80 ± 0.02	$0.34^{+0.10}_{-0.13}$	0.58	712/713	699
04	00030090004	91423-01-01-04	$0.24^{+0.00}_{-0.01}$	66358	1.86 ± 0.01	0.27 ± 0.06	1.06	870/757	1503
03	00030090003	91094-01-01-04	$0.25^{+0.00}_{-0.01}$	63806	$1.86^{+0.00}_{-0.02}$	$0.35^{+0.05}_{-0.08}$	1.06	544/548	1024
07	00030090007	91094-01-02-01	$0.24^{+0.01}_{-0.00}$	69967	$1.83^{+0.02}_{-0.01}$	$0.36^{+0.04}_{-0.08}$	1.16	702/679	1112
06	00030090006	91094-01-02-01	$0.24^{+0.00}_{-0.01}$	83839	$1.82^{+0.02}_{-0.01}$	$0.32^{+0.08}_{-0.07}$	1.26	868/762	1674
10	00030090010	91094-01-02-00	$0.25^{+0.00}_{-0.01}$	70377	$1.82^{+0.01}_{-0.02}$	$0.33^{+0.03}_{-0.04}$	1.17	752/726	2192
08	00030090008	91094-01-02-00	0.28 ± 0.02	36514	1.81 ± 0.01	$0.28^{+0.05}_{-0.04}$	0.86	275/273	232
09	00030090009	91094-01-02-00	$0.24^{+0.01}_{-0.00}$	73119	$1.81^{+0.01}_{-0.01}$	0.28 ± 0.05	1.17	873/784	2955
11	00030090011	91094-01-02-02	0.25 ± 0.02	59219	1.81 ± 0.01	0.29 ± 0.06	1.02	333/320	250
12	00030090012	91094-01-02-02	$0.23^{+0.01}_{-0.00}$	79673	1.81 ± 0.01	$0.29^{+0.05}_{-0.06}$	1.09	860/746	1898
13	00030090013	91094-01-02-02	$0.23^{+0.01}_{-0.00}$	75104	1.81 ± 0.01	0.30 ± 0.06	1.08	622/633	1134
15	00030090015	91094-01-02-03	$0.23^{+0.00}_{-0.01}$	69620	1.79 ± 0.01	$0.31^{+0.07}_{-0.06}$	0.99	818/743	1231
16	00030090016	91094-01-02-03	0.25 ± 0.01	49618	1.79 ± 0.01	$0.31^{+0.06}_{-0.07}$	0.94	717/655	1030
18	00030090018	91423-01-03-06	$0.23^{+0.01}_{-0.02}$	42447	1.73 ± 0.01	0.24 ± 0.06	0.64	396/435	347
19	00030090019	91423-01-04-02	0.22 ± 0.01	39291	1.72 ± 0.01	$0.28^{+0.07}_{-0.06}$	0.57	626/646	732
20	00030090020	91423-01-06-00	$0.23^{+0.01}_{-0.02}$	17415	$1.67^{+0.02}_{-0.01}$	$0.20^{+0.07}_{-0.09}$	0.36	433/460	178
21	00030090021	91423-01-08-02	0.22 ± 0.02	9122	1.65 ± 0.03	$0.19^{+0.16}_{-0.17}$	0.21	514/518	50
23	00030090023	91423-01-10-00	0.17 ± 0.02	14876	$1.65^{+0.01}_{-0.02}$	$0.16^{+0.05}_{-0.09}$	0.18	635/659	32
24	00030090024	91423-01-11-00	$0.16^{+0.02}_{-0.03}$	16135	$1.67^{+0.01}_{-0.02}$	$0.24^{+0.11}_{-0.13}$	0.16	602/631	19
26	00030090026	91423-01-13-00	$0.17^{+0.05}_{-0.10}$	4629	$1.63^{+0.02}_{-0.04}$	$0.13^{+0.14}_{-0.13}$	0.11	559/562	4
30	00030090030	91423-01-16-01	$0.04^{+0.05}_{-0.03}$	934	$1.64^{+0.01}_{-0.02}$	$0.09^{+0.14}_{-0.09}$	0.11	559/592	3
31	00030090031	91423-01-17-00	$0.13^{+0.04}_{-0.12}$	13157	$1.63^{+0.02}_{-0.03}$	$0.14^{+0.16}_{-0.14}$	0.10	576/508	3

Table 3.1: The table details the datasets we use from *Swift* and *RXTE*. We refer to the combined spectrum by the last two numbers of its *Swift* obsID. The remaining columns give the results for fitting the 0.5-200 keV X-ray data with a `wabs*(diskbb+thCompml)` model with the absorption fixed at 0.2×10^{22}, seed photons for the Comptonisation tied to the disc temperature and reflection assumed to be from solar abundance material inclined at 60°. Column 9 shows the resulting χ^2 for the fit, and the final column is the difference in χ^2 for removing the disc and putting the seed photon energy for the Compton scattering to 0.1 eV
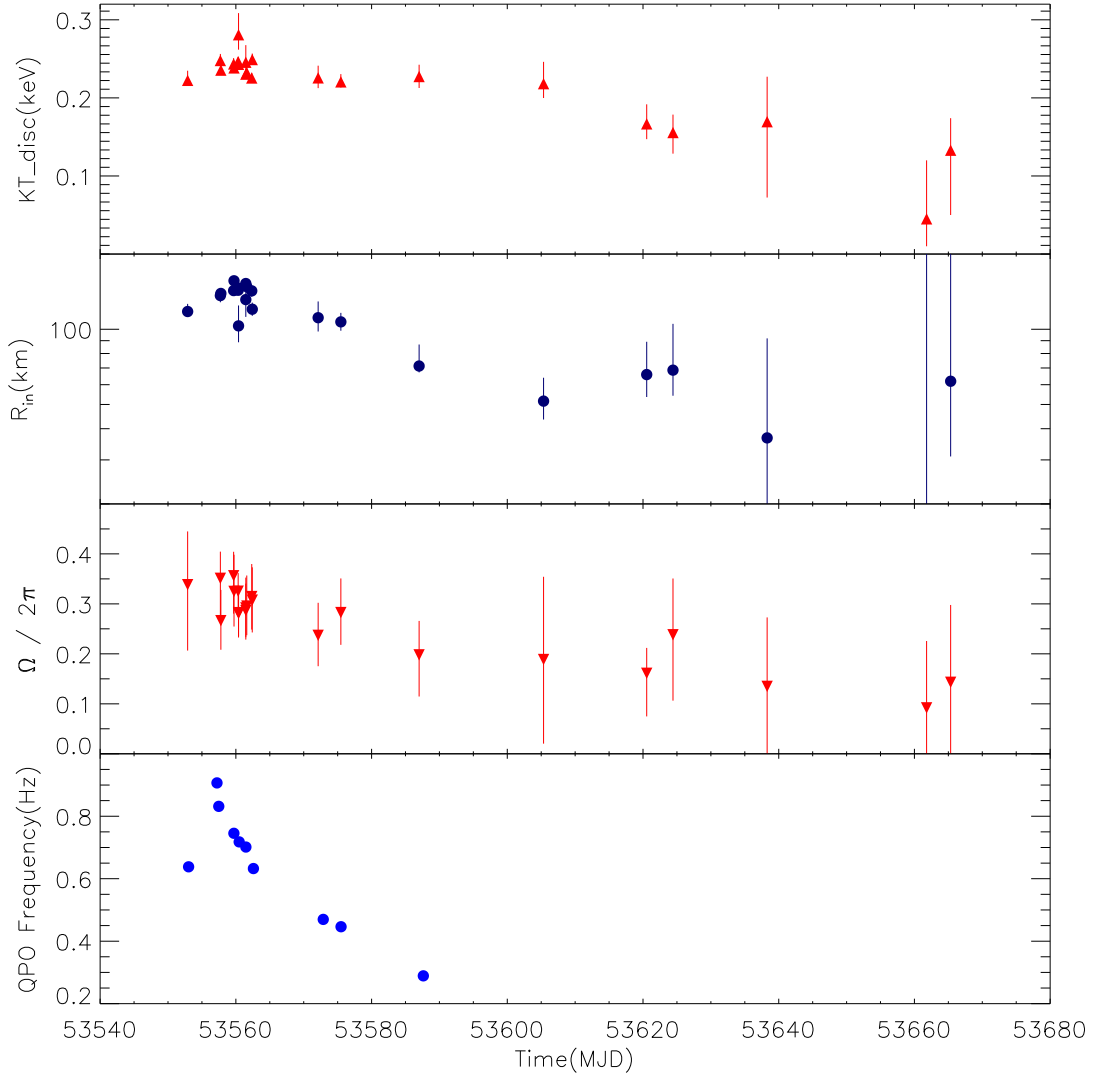
Figure 3.1: The plot shows the results of the disc temperature, inner radius and reflection evolution obtained from the `diskbb+thCompml` model. The value of inner radius were derived from the `diskbb` normalisation assuming an inclination of 60° [+] and distance of 5.4kpc. As these are poorly known, the absolute value of the radius is not well constrained. However, trends should be robust, and clearly the derived inner radius remains constant or mildly decreases during the outburst. This is in sharp contrast to the expected increase from truncated disc models. Reflection (third penal) and the QPO frequency (lower panel, see also Table 2.1), on the other hand, decreases when leaving the peak, as expected if the disc is receding.

(a)   (b)   (c)

Figure 3.2: The unabsorbed data and X-ray model fit (`diskbb + thCompml`) at the outburst peak (top panel, spectrum 10), midway down the decline (middle panel, spectrum 20) and in the outburst tail (lower panel, spectrum 30). The magenta and blue components are disc emission and Comptonisation in corona, respectively.

in the optical/UV for these data. Thus X-ray reprocessing from hard X-ray illumination of the outer disc seems the most likely origin for the optical/UV flux (van Paradijs 1996).
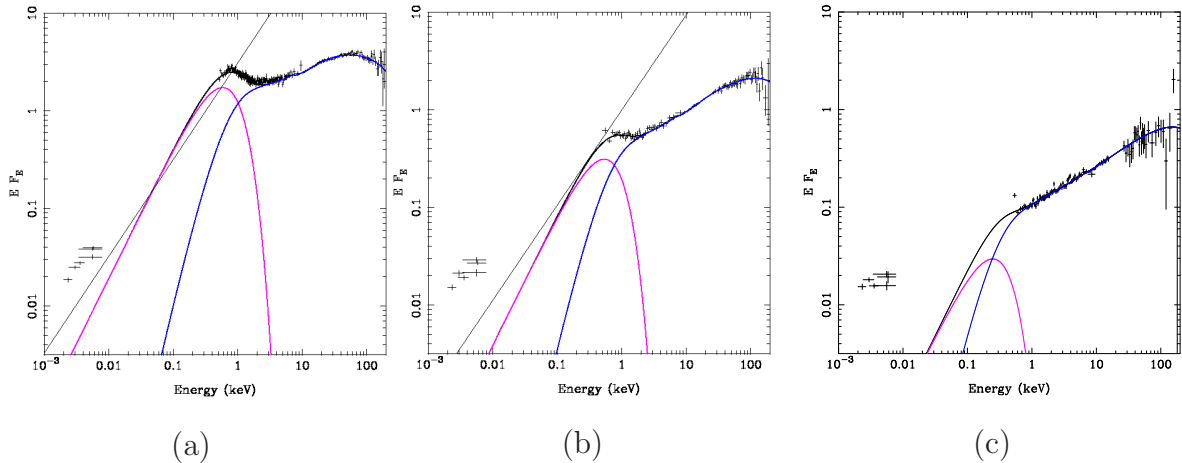
There are additional radio observations from midway down the outburst decline (Cadolle Bel et al. 2007). Figure 3.2b shows this radio emission, extrapolated as above, onto spectrum 20, the dataset closest in time to the radio observations. Again, the optical/UV points are not fit by either the hard X-ray power law extrapolated down (though this time the mismatch is not so large), or by the radio emission extrapolated up, or by the disc inferred from the soft X-ray component, as also shown in Cadolle Bel et al. (2007).

Figure 3.2c shows a spectrum from the end of the outburst (30), where there are no radio observations. The disc emission fit to the soft X-ray component is now very weak and cool, and its extrapolation down to the optical lies dramatically below the observed optical/UV emission. However, the optical/UV emission does lie remarkably close to the
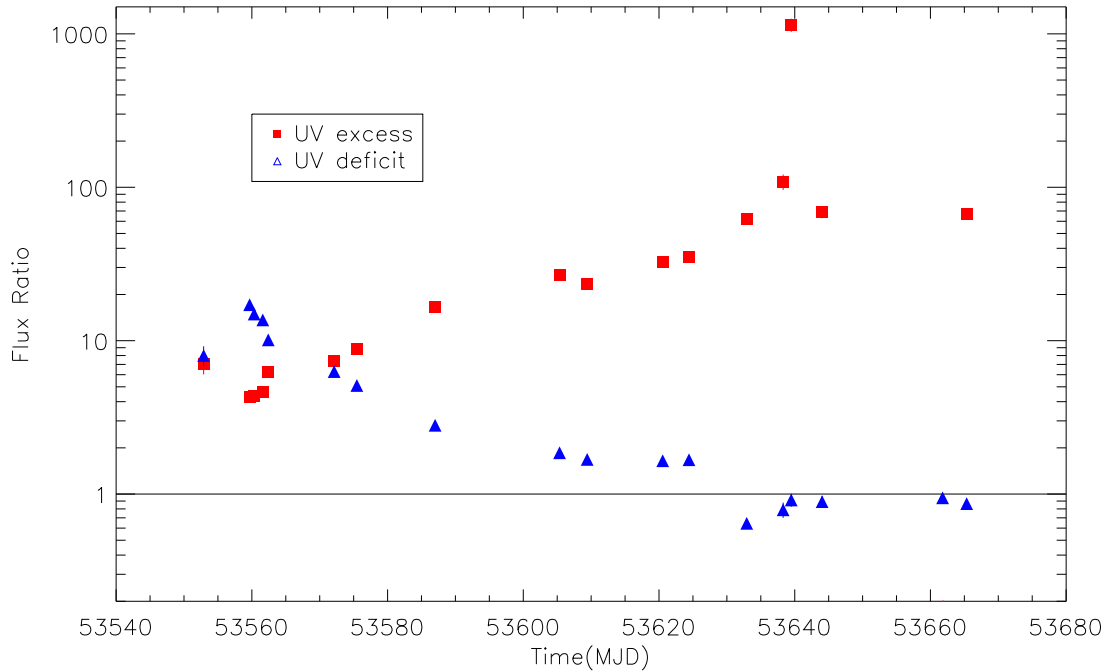
Figure 3.3: The red squares show the evolution of UV excess i.e. the observed UVW1 flux divided by the UVW1 flux predicted by the model fit to the soft X-ray disc. This always underpredicts the observed UVW1 emission, by an amount that increases as the source fades. The soft X-ray disc component is not significant in the final 3 points but the trend is already clear even without these data. The blue triangles show the 'UV deficit' i.e. the ratio of model to observed flux in the UVW1 filter predicted from extrapolating the `thCompml` continuum down into the optical assuming the seed photons are at 0.1 eV rather than from the disc. Close to the peak of the outburst this UV deficit is large, showing that the X-rays over-predict the UV flux. Conversely, towards the end of the outburst, the UV data lie very close to the extrapolation of the hard X-ray flux.

extrapolated hard X-ray flux in these low-luminosity data.

We quantify this by calculating the factor by which the disc component underpredicts the observed flux in the UVW1 filter ('UV excess': GDP09) in each spectrum. We also calculate a 'UV deficit', which is the factor by which the Comptonisation model *overpredicts* the flux in the UVW1 filter if its seed photons put at 0.1 eV rather than fixed to the disc temperature. Such low energy seed photons may be produced by cyclo-synchrotron emission by the same thermal electrons which produce the Compton scattered emission interacting with the tangled magnetic field in the hot flow itself (Narayan and Yi 1995; di Matteo et al. 1997; Wardziński and Zdziarski 2000). Figure 3.3 shows how these evolve during the outburst. This confirms the results seen in the three individual spectra discussed above. The 'UV excess' (red triangles) increases strongly with time, as the soft X-ray disc component makes less and less contribution to the UV flux. The disc is not significantly detected in the final three spectra, but the trend in UV excess is already clearly apparent. Conversely, the UV deficit (blue squares) decreases, and is roughly consistent with the observed UV flux from spectrum 21 onwards.

3.3 Irradiated Disc Model

We first look at the possibility that irradiation of the disc is responsible for all the issues highlighted in the previous section. Irradiation of the inner disc can change its temperature and radius compared to that derived from fitting purely gravitational energy release models of the disc. Similarly, irradiation of the outer disc can also increase the optical/UV emission from that expected from an unilluminated disc.

We use a slightly modified version of the `diskir` model of GDP08 so that the disc temperature and normalisation are set by the physical variables of the mass, distance, mass

(a)　　　　　　　　　　　　　　　　(b)
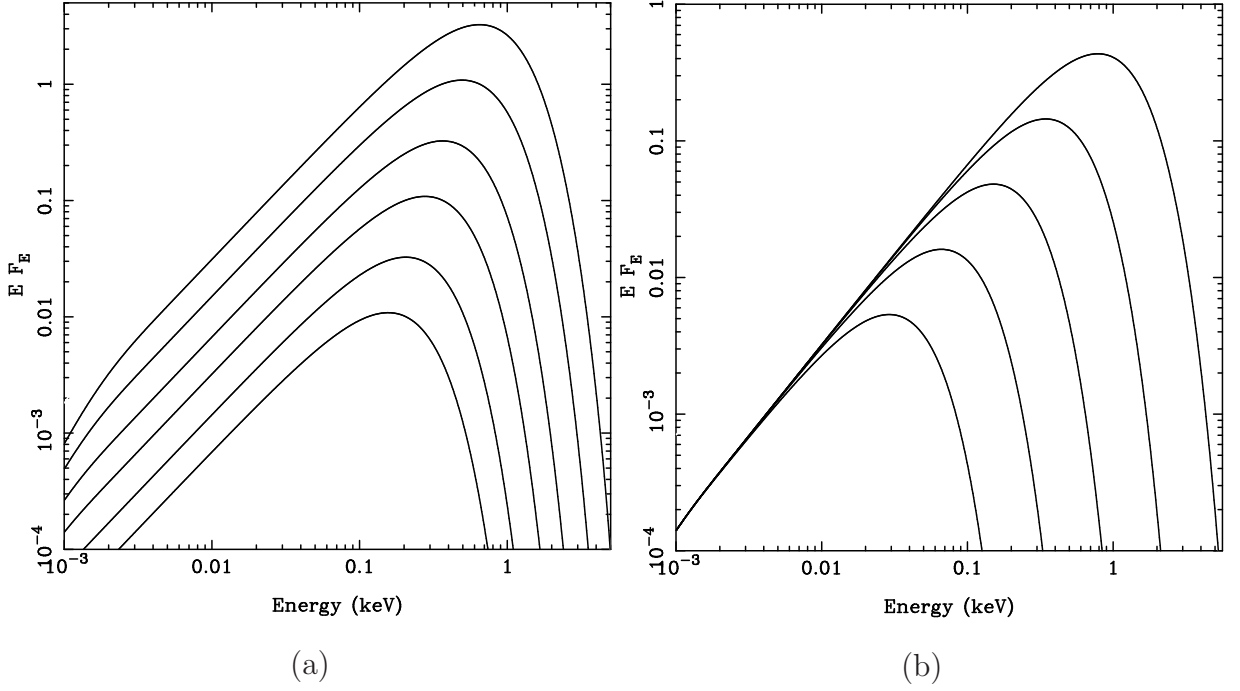
Figure 3.4: Irradiated disc model with no Comptonized tail (i.e. $L_c = 0$) and a fixed outer radius ($R_{out} = 10^5\ R_g$), as a function of mass accretion rate (left panel) and the inner radius (right panel), both without inner and outer reprocessing.(a)Inner radius = 20 R_g. Curves from bottom to top show the increasing mass accretion rates, which are $10^{16}, 3 \times 10^{16}$, 10^{17}, 3×10^{17}, 10^{18}, and 3×10^{18}, respectively. (b)All the curves are at $\dot{m} = 10^{17} g/s$. Inner radius from top to bottom is 5 R_g, 15 R_g, 45 R_g, 135 R_g, and 405 R_g.

accretion rate and inner and outer radii. This has the advantage that the outer radius is set in terms of physical units, rather than relative to the (possibly changing) inner radius as in `diskir`. We parameterise the inner and outer radii in terms of $R_g = GM/c^2$, and leave the inner radius as a free parameter in the fits. We fix the mass and distance at the best (though poorly constrained) estimates of 12 $M_\odot$ and 5.4 kpc, respectively (Zurita et al. 2008).

Figure 3.4(a) shows the disc model spectra at different mass accretion rates. As the
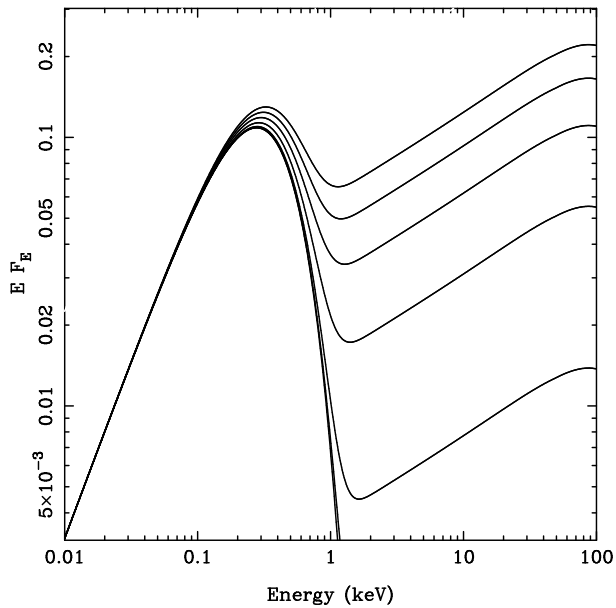
Figure 3.5: Irradiated disc model as a function of L_c/L_d. This is at $\dot{m} = 10^{17}g/s$, $R_{in} = 20\ R_g$ and $R_{out} = 10^5\ R_g$. The model was calculated for $\Omega/2\pi = 0$, $f_{out} = 0$, $\Gamma = 1.7$ and $kT_e = 100$ keV. From bottom to top the L_c/L_d increases from 0, 0.05, 0.25, 1, 2, 3 to 4.

mass accretion rate increases, the disc emission increases everywhere and peaks at higher energy, but the peak energy is also related to the inner edge of the disc. Allowing the disc to expend down to smaller radii increases the high energy emission from the disc, but the lower energy emission remains the same for the same mass accretion rates and a fixed outer radius (shown in Figure 3.4(b)). However there is also a corona as well as the disc which forms the hard X-ray contribution. This is parameterised in terms of its luminosity L_c with respect to the intrinsic disc emission, L_d. As L_c/L_d increases, the hard X-ray component becomes more and more dominant (see Figure 3.5). Some fraction of this disc plus coronal emission will illuminate to the inner and outer disc. Spectra with irradiation are shown in Figure 3.6, whose panel (a) shows the effect of irradiation on the inner disc from a region where the hot flow overlaps with the cool disc. The illuminated inner disc has a higher temperature so peaks at higher energy, and the soft X-ray emission

(a)

(b)
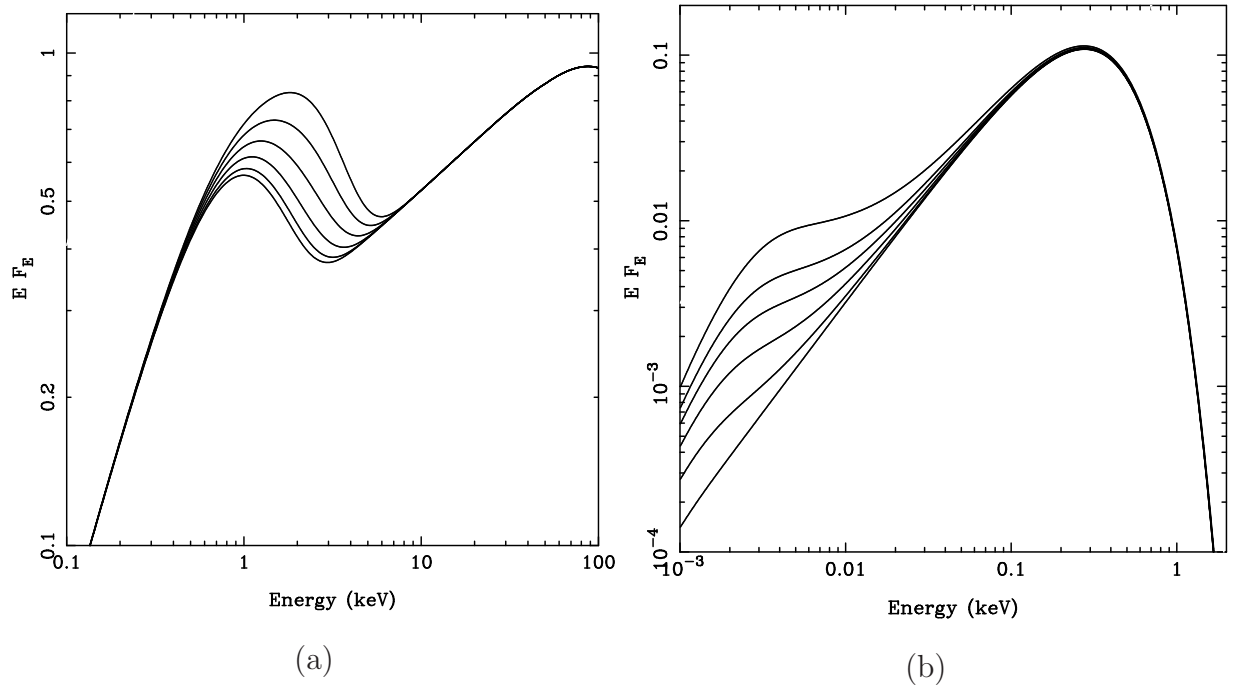
Figure 3.6: Irradiated disc model as a function of inner irradiation fraction (left panel) and outer irradiation fraction (right panel). Both panels are at $\dot{m} = 10^{17} g/s$ and $R_{out} = 10^5$ R_g. f_{in} and f_{out} state the amount of irradiation on inner disc and outer disc. Their values are between 0 and 1, where 0 means the corona does not illuminate the disc and cause a higher surface temperature than that caused only by intrinsic thermal viscosity. (a)The model was calculated for $R_{in} = 5\ R_g$, $f_{out} = 0$, $L_c/L_d = 4$ and $\Gamma = 1.7$. From bottom to top the f_{in} increases from 0, 0.01, 0.03, 0.06, 0.1 to 0.15 for an illuminated region of radius $1.1 \times R_{in}$.(b)From bottom to top, $f_{out} = 0$, 0.001, 0.003, 0.006, 0.01 and 0.02, respectively.

also increases. But f_{in} can only shift peak energy as the inner radius is close to the black hole, otherwise the effect is not obvious. Figure 3.6(b) shows the effect of irradiation on the outer disc, increasing the amount of optical emission from reprocessing.

We assume the outer radius should remain constant, as should the absorption (but see Cabanac et al. 2009) so we try to constrain both of these by simultaneously fitting three
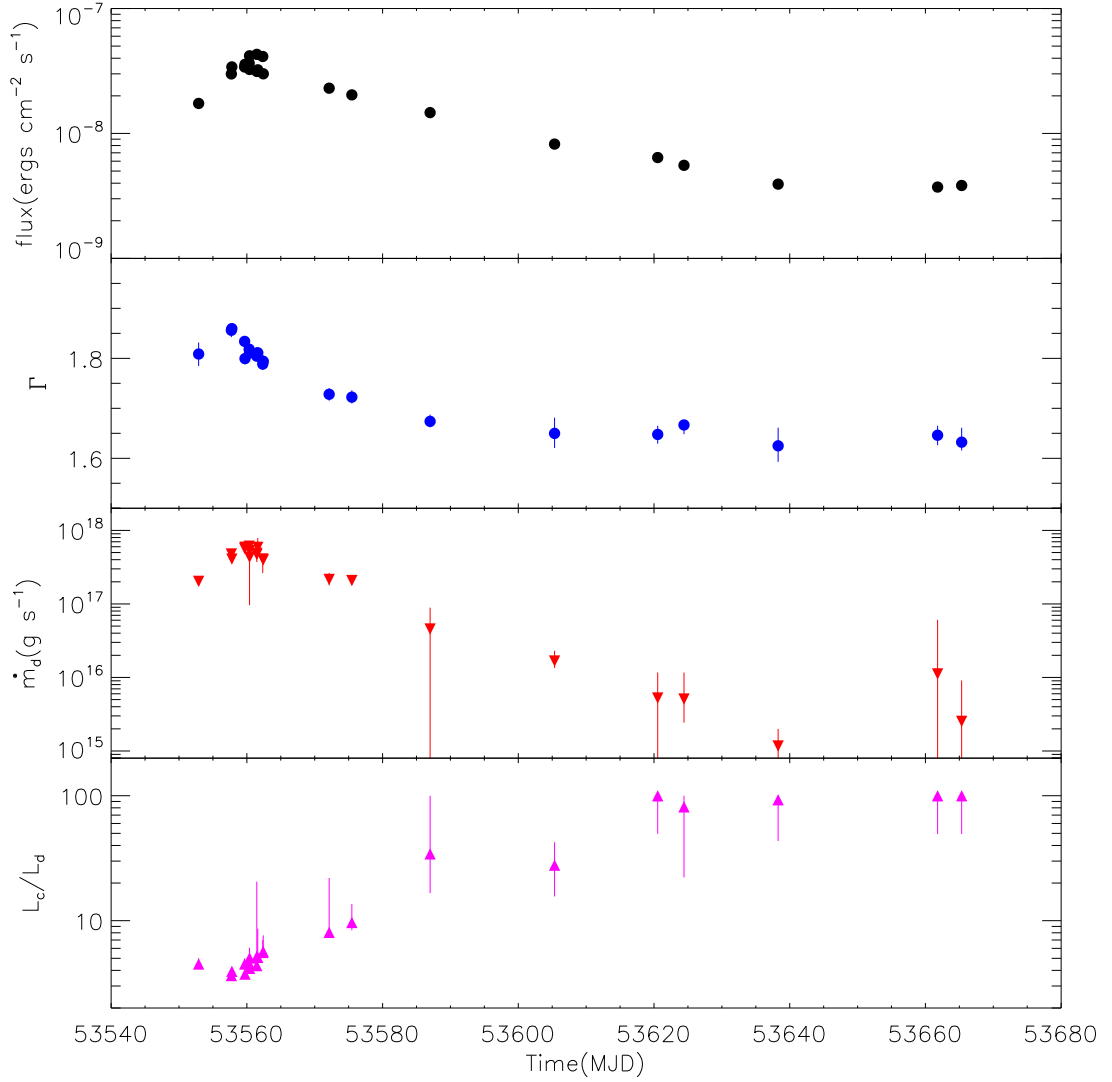
Figure 3.7: Evolution of an irradiated disc model fit to the optical/UV/X-ray spectrum. The top panel shows the bolometric flux, taken from the unabsorbed model integrated between 0.001-100 keV. This drops by a factor of 10 during the outburst, close to that seen from the X-ray emission alone in Fig. 1. The second panel shows the hard X-ray spectral index, which softens from 1.8 to 1.6. The third panel shows the mass accretion rate $\dot{m}_d$ required to power the intrinsic (gravitational) emission from the disc luminosity, $L_d = GM\dot{m}_d/2R_d$. This drops by nearly two orders of magnitude, so the ratio of this to hard X-ray luminosity in the corona L_c/L_d increases by a factor 10 (fourth panel). The intrinsic disc luminosity is enhanced by irradiation of the inner disc by the hard X-ray corona.
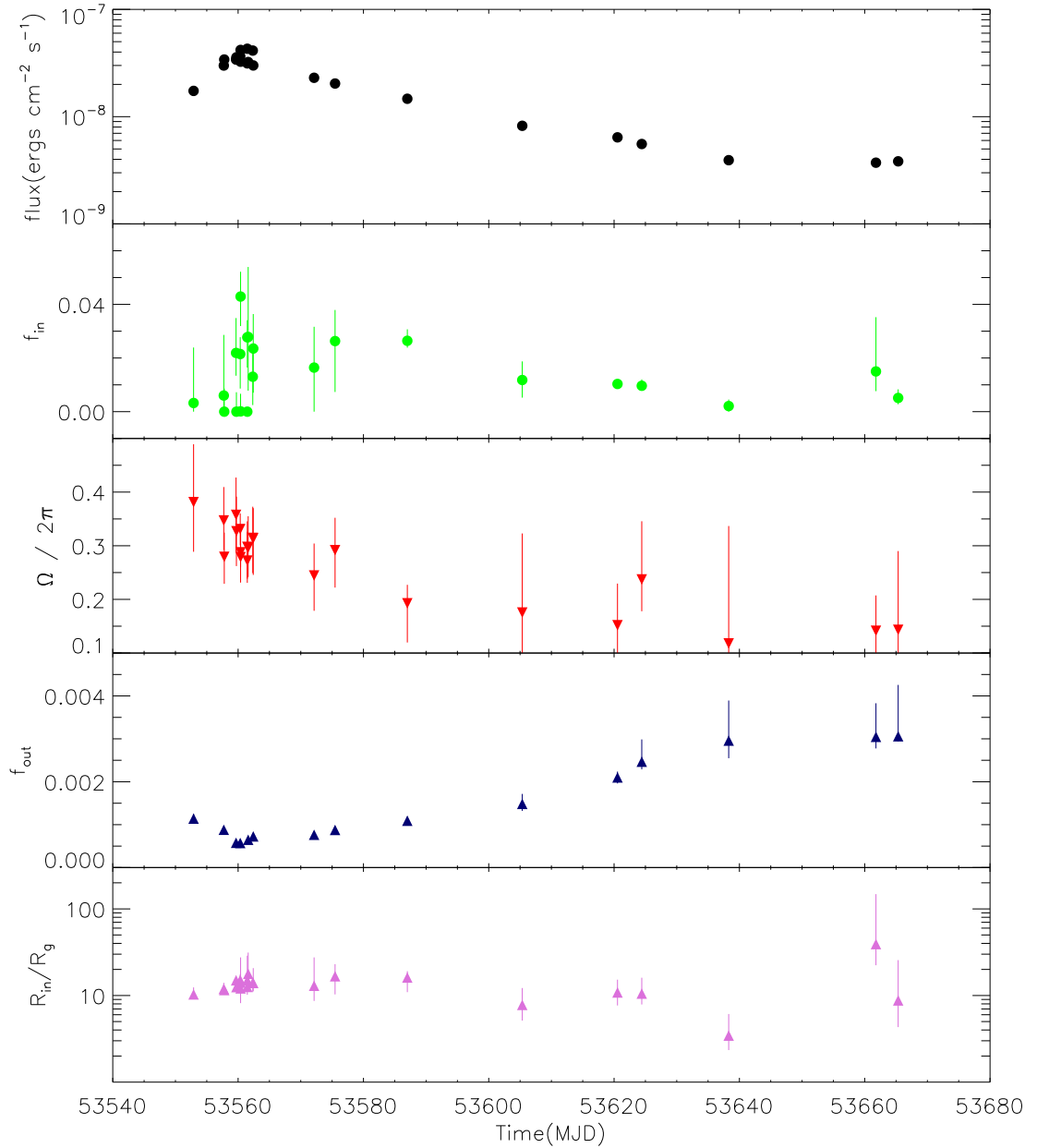
Figure 3.8: Continued evolution of an irradiated disc model fit to the optical/UV/X-ray spectrum. The fraction of irradiation required drops during the decline (second panel) as does the amount of (neutral) reflected emission (third panel). The fourth panel shows the fraction of the bolometric flux which is required to thermalise in the outer disc in order to make the observed optical/UV flux. This strongly increases during the decline (see also Figure 3.3). The final panel shows the inferred inner radius of the disc. This remains remarkably constant in this model at around 10 R_g (see also Figure 3.2). Such a small inner disc radius at the end of the decline is in conflict with the truncated disc model predictions. It is also inconsistent with limits on reprocessed emission (see discussion). If instead there is a separate soft X-ray component (see Figure 3.11) as required in the similarly dim low/hard state spectra from XTE J1118+480 then these data do not constrain the disc radius.

datasets from various points in the outburst with the `diskir` model together with X-ray absorption parameterised by `wabs` and UV reddening by `redden`. Assuming standard gas to dust ratios allows us to tie $E(B-V) = 1.5 \times N_H/10^{22}$ (GDP08). This gives a best fit at $N_H = 2.1 \times 10^{21} cm^{-2}$ and $R_{out} = 10^{5.25} R_g$, which are fixed to these values in all fits hereafter. The value of R_{out} is bigger than the estimated theoretical value ($\sim 10^4.8$), but since the mass is highly uncertain, we think the result obtained from the data is more reliable.

3.3.1 Evolution of the irradiated disc model parameters

We fit this model to all the *Swift-RXTE* datasets. Guided by previous low/hard state data (Poutanen et al. 1997; GDP08), we fix the radius of the irradiated portion of the inner disc at $1.1 \times R_d$. Figure 3.7 and 3.8 show the evolution of the source parameters in this model. The top panel gives the bolometric flux, which varies by an order of magnitude. This is dominated by the hard X-ray component, whose spectral index (second panel in Figure 3.7) decreases from 1.8 to 1.6 during the first section of the decline, and then stabilizes at this value hereafter. The source did not make a transition to the high/soft or even intermediate state, but remained in the hard state throughout the outburst.

The disc spectrum forms a component which connects the soft X-ray rise to the optical emission in this model. Part of this is powered by gravitational energy release, and the inferred mass accretion rate through the disc decreases by more than 2 orders of magnitude during the decline (third panel in Figure 3.7). Thus the ratio of the hard X-ray flux to this inferred intrinsic disc flux increases by an order of magnitude (fourth panel in Figure 3.7).

The intrinsic gravitational energy of the disc is augmented by thermalisation of the

(a)   (b)   (c)
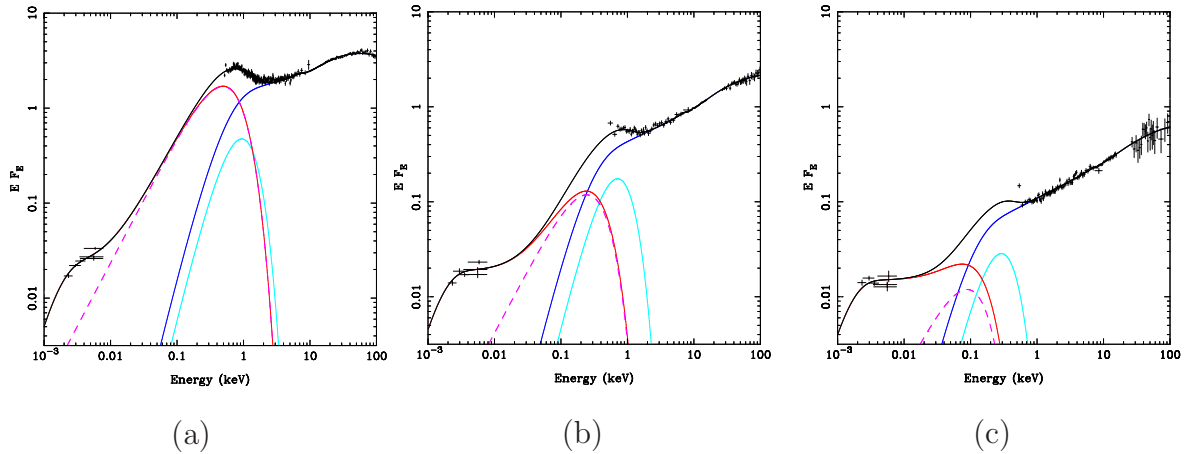
Figure 3.9: The same 3 spectra (10, 20 and 30) as in Fig. 3, fit with the irradiated disc model and corrected (data and model) for absorption. The magenta dashed line is the intrinsic disc emission, the red line includes irradiation of the outer disc, and the cyan line shows the additional flux from irradiation of the inner disc. The Comptonised emission and its reflected spectrum are shown in blue. While the inner disc irradiation, fin, drops, the increase in L_c/L_d means that the total disc spectrum is more distorted by irradiation at lower fluxes.

irradiating flux on the inner disc. The fraction of the hard X-ray spectrum which illuminates the *inner* disc and is thermalised basically decreases during the decline (second panel in Figure 3.8), as expected if the inner edge of the disc is receding. Similarly, the amount of hard X-ray reflection also declines (third panel in Figure 3.8). Conversely, the fraction of hard X-rays which thermalise in the *outer* disc increases by almost an order of magnitude (fourth panel in Figure 3.8). The final panel of Figure 3.8 shows the disc inner radius. This is plainly consistent with a more or less constant value, although the error bars become large at later stages of the decline. Figure 3.9 show the corresponding fits to the data of Figure 3.2a-c for this model.
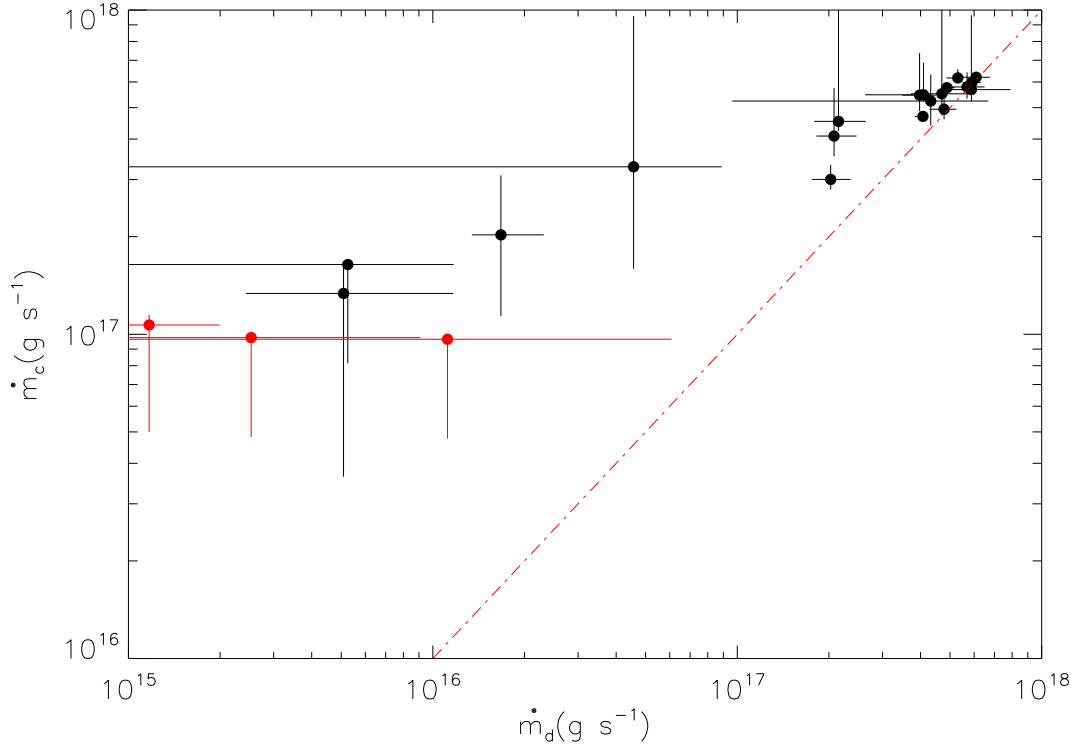
Figure 3.10: Irradiated disc model mass accretion rate through the disc, $\dot{m}_d$ versus that through the corona, $\dot{m}_c$, derived from $(L_c/L_d)(R_d/R_c)\dot{m}_d$, with $R_c = 3.5 \ R_g$ fixed by requiring $\dot{m}_c \approx \dot{m}_d$ (shown by the red dashed line) for the brightest spectra. The red points show the 3 faintest spectra where there is no significant additional soft X-ray component. Even without these spectra the trend is clear that $\dot{m}_c$ gets progressively larger than $\dot{m}_d$ as the source declines. This is opposite to the expected trend from a radiatively ineffcent flow. are away from the line.

3.3.2   Inferred mass accretion rate

We can use these derived parameters to explore how the mass accretion rate through the disc compares to that required to power the hard X-rays. We calculate the mass accretion rate of the corona by:

$$L_c = \frac{\eta_{corona}}{\eta_{disc}} \frac{GM\dot{m}_c}{2R_c},$$

(3.1)

where $\eta_{corona}/\eta_{disc}$ is the relative efficiency of converting mass to radiation in a coronal flow which extends down to R_c versus that in a disc extending down to the same radius. However, the disc itself only extends down to a radius R_d so its luminosity from gravitational energy release alone is $L_d = \frac{1}{2}GM\dot{m}_d/R_d$. Thus

$$\frac{L_c}{L_d} = \frac{\eta_{corona}}{\eta_{disc}} \frac{\dot{m}_c}{\dot{m}_d} \frac{R_d}{R_c}.$$

(3.2)

The spectral fitting parameters give L_c/L_d, $\dot{m}_d$ and R_d. Close to the peak of the outburst, even a radiatively inefficient flow should have $\eta_{corona}/\eta_{disc} \sim 1$. Here we also expect $\dot{m}_c \sim \dot{m}_d$, which requires R_c to be around 3 times smaller than R_d at this point. For our assumed values of the mass and distance this gives $R_c = 3.5R_g$. We can then calculate $\dot{m}_c$ assuming $\eta_{corona}/\eta_{disc}$ and R_c remain constant. This is plotted against $\dot{m}_d$ in Figure 3.10. The red line is $\dot{m}_c = \dot{m}_d$, showing clearly that these models favour a larger mass accretion rate through the corona than through the disc on the decline. This conclusion is strengthened if the flow is increasingly radiatively inefficient at lower mass accretion rates, as the observed X-ray flux would then require an even larger coronal mass accretion rate to power the same amount of hard X-ray emission.

This conclusion is driven by the *observational* requirement for a soft X-ray component in the late state decline data. This is weak, but significantly present in all but the last

three datasets (assuming that the absorption column remains constant: Cabanac et al. 2009). It combines a low luminosity with a fairly high (soft X-ray) temperature, which leads to the derived small radius and low mass accretion rate. This low mass accretion rate is then much smaller than that required to power the observed hard X-ray emission.

We illustrate this by re-coding the irradiated disc model to force $\dot{m}_c = \dot{m}_d$ for $R_c = 3.5R_g$, for $\eta_{corona}/\eta_{disc} = 1$. This forces the disc to have a higher mass accretion rate, so it must truncate at a larger radius so as not to overproduce the observed soft X-ray component. Irradiation of the inner disc should then be negligible, so we fix $f_{in} = 0$ for physical consistency, and we focus first on the X-ray data alone so we also fix $f_{out} = 0$.

We fit this to spectrum 24 (the lowest luminosity data for which the disc is significantly detected in the soft X-ray flux), and first focus on the X-ray data alone. The mass accretion rate through the disc is much higher ($1.2 \pm 0.1 \times 10^{17}$ g/s compared to 1.0×10^{16} in the `diskir` fits) and the disc inner radius increases to 30 R_g from ~ 5 R_g. This disc contributes to the spectrum only at the softest energies of the *Swift* XRT, and its sharp rise is rather different to the more gradual curvature seen in the soft X-ray emission. Thus this gives a significantly worse fit ($\chi^2_\nu = 626/632$ versus $600/630$, where the two extra free parameters are L_c/L_d and f_{in}). We can only recover the same quality of fit with $\dot{m}_d = \dot{m}_c$ by including an additional soft component. This allows the disc to recede back even further, to ~ 50 R_g, so that the truncated disc makes no contribution to the soft X-ray flux. Figure 3.11 shows this fit including now the optical/UV data with $f_{out} = 2 \times 10^{-3}$ (similar to that derived from the original fits, see Figure 3.8).

Irradiation can make such a hot, weak component if the irradiated disc area is *small*. We fixed the radius of the reprocessing region at $1.1 \times R_d$ for the fits in Figure 3.7 and 3.8, but as the disc recedes then the changing geometry means that this should also drop.
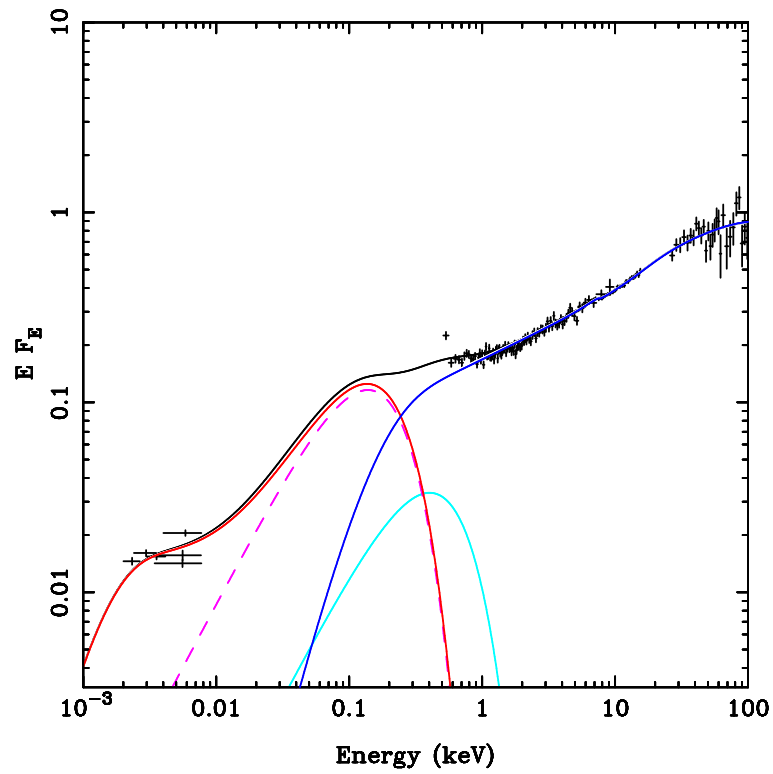
Figure 3.11: Spectrum 24 fit by a model where $\dot{m}_d = \dot{m}_c$ and a separate component (cyan, modelled with `diskbb`) to fit the soft X-ray emission. The observed strong X-ray flux requires a large mass accretion rate through the disc, so this has to truncate at $\sim 50\ R_g$, forming the UV peak, so as not to overproduce the soft X-ray emission.

We allow this to be a free parameter with $\dot{m}_c = \dot{m}_d$ and can recover as good a fit as before ($\chi^2 = 601/632$) with ~ 1 per cent of the bolometric flux being reprocessed in a region with $R_{irr} = 1.002R_d$. However, illumination of such a tiny area of the disc surface seems unreasonable from illumination by a central source.

Chapter 4

Discussion

4.1   Outburst Peak

The soft X-ray component seen at the peak of the hard state during the outburst of SWIFT J1753.5-0127 is clearly from the disc. While the system parameters are rather poorly known, the radii derived close to the peak are $\sim 15\ R_g$, consistent with the disc being slightly recessed back from the last stable orbit, as required for the truncated disc/hot inner flow interpretation of the hard state. There are two independent lines of support for this number. The first comes from the fact that the hard X-ray spectrum is softer close to the peak, clearly consistent with the disc providing an increasing source of seed photons to Compton cool the hot X-ray plasma. Since most of the gravitational potential energy to power this corona is concentrated within $20 R_g$ then it seems most likely that the disc extends down to similarly small radii. This means that there can also be irradiation of the inner disc by the hard X-ray emission, leading to reflection and thermalisation of the incident flux. We see evidence for both these processes in the spectrum, with the extra flux from irradiation increasing the inferred disc radius from the value of $\sim 11\ R_g$ inferred from the simple (unirradiated) disc fits to the X-ray spectrum, to $15\ R_g$. The second is from low frequency QPO which is at its maximum of ~ 0.9 Hz in these data (see Table **??**). This implies an outer radius of $\sim 25\ R_g$ assuming that the QPO is produced by Lense-Thirring (vertical) precession of the hot flow (Ingram et al. 2009).

The mass accretion rate required to power the disc emission is comparable with that

required to power the coronal hard X-ray emission assuming that the corona extends down to a radius which is ~ 5 times smaller than that of the disc i.e. $3.5R_g$ for the parameters assumed here. While we stress again that these system parameters are poorly known, such a small number is potentially feasible for a hot inner flow, irrespective of the spin of the black hole, as numerical simulations of the MRI turbulence show that the large scale height magnetic fields can extract energy from the infalling material beyond the last stable orbit (e.g. Krolik et al. 2005).

The optical emission is most likely dominated by X-ray illumination of the outer disc as is clearly seen in high/soft state data for BHB (GDP09). This is confirmed by the correlated variability of the optical and X-ray flux (Hynes et al. 2009), clearly showing that the optical is lagged and smeared, as expected from reprocessing.

4.2 Late Stage Decline

The outburst peak spectra then form a template for comparison with the later stages of the decline, where the bolometric flux is lower by a factor 10. The truncated disc/hot inner flow model makes a clear prediction that these should have a larger inner disc radius, decreasing the importance of illumination on the inner edge of the disc, and decreasing the amount of associated reflection. Thus illumination of the surface of the disc is not expected to be important in distorting the derived inner disc radii in these spectra. Similarly, as there is lttle (or no) overlap in radii between the hot inner flow and disc, so the disc emission cannot be strongly suppressed by Comptonisation as can be the case close to the transition (Kubota and Done 2004; Makishima et al. 2008). Thus any disc component seen in these spectra should give a fairly unbiased view of the inner radius of the flow. Yet associating the observed soft X-ray component with this disc gives derived radii which are as small, if not smaller than, the radii seen at the outburst peak, in clear

conflict with the truncated disc models (see Figure 3.2 and Figure 3.8).

However, these small radii are themselves in more subtle conflict with the observations. The small disc has very small luminosity compared to the coronal emission. This requires that the coronal mass accretion rate must be large compared to that through the disc if the corona is powered by matter accreting through it. Thus the corona cannot be predominantly fed by material evaporating from the inner edge of the disc, but instead requires a completely separate coronal flow which incorporates most of the incoming mass accretion from the companion star. Yet it seems quite unlikely that the incoming cool Roche lobe overflow stream would be able to form such a coronal flow at large radii.

Instead it seems more feasible that the corona is *not* powered by its own mass accretion supply, as in the truncated disc models, but is instead powered by mass accreted through the disc, but whose energy is released in the corona (e.g. Svensson and Zdziarski 1994). However, this model itself runs into difficulties since the simplest idea would be for magnetic buoyancy to transport the energy vertically. The energy is then released in a corona above the disc, so the corona is co-spatial with it and illuminates it. This gives rise to a reprocessed luminosity $L_{rep} = \frac{1}{2}(1 - a)L_c$ (where a is the albedo, and the factor $\frac{1}{2}$ assumes the corona emitts isotropically) adds to the intrinsic disc luminosity (Haardt and Maraschi 1993). For hard spectra, such as those observed here, the reflection albedo $a < 0.3$, hence the disc flux should be at least $L_c/3$. Yet we observe a disc flux of $\leq L_c/20$ towards the end of the outburst. Thus the only way to circumvent the reprocessing limits whilst having all the mass accrete via the disc is if the energy is advected radially as well as vertically. Then it can be released in a more centrally concentrated region, on size scales smaller than the (small!) disc inner radius. The alternative of having the hard X-rays be strongly beamed away from the disc, is ruled out by the very similar dim low/hard state spectra seen in XTE J1118+480 (Frontera et al. 2001; 2003; Reis, Miller

and Fabian 2009), which has high inclination ($\geq 70°$) so that we must see a similar hard X-ray flux to that of the disc.

A potentially less arbitrary solution than using magnetic fields to transport the energy in a dissipationless fashion is if the observed soft X-ray component in the late stages of the decline is not from the disc. The spectra clearly show that the observed soft X-ray emission cannot produce the optical/UV emission without a large change in the reprocessed fraction in the outer disc from that seen during the outburst peak. Yet the outburst remained in the low/hard state, so there is no expected change in source geometry, so the fraction of the total flux which illuminates the outer disc should not change dramatically. Similarly, there is no large change in spectral shape which might produce such a large difference in thermalisation fraction. Yet the observed soft X-ray component is a factor 10 further below the UV emission than at the outburst peak (Figure 3.3). This could be used to argue that the real disc is truncated, as in Figure 3.9, so is larger and cooler, so that the same amount of reprocessing can produce the optical/UV.

However, it is clear that the optical/UV emission does change character during the decline. The rapid variability of the optical flux changes dramatically during the decline, switching to an anti-correlation of the optical and X-ray emission (Hynes et al. 2009). Clearly this shows that the optical is no longer made predominantly by reprocessing of the hard X-ray flux, so it gives only an upper limit to the irradiated disc flux.

Thus the optical emission does not trace the outer disc, so cannot constrain our inner disc models. Instead, we use the similarly dim low/hard state spectra from XTE J1118+480. to argue for a non-disc origin for the soft X-ray component. These have an absorption column which is an order of magnitude lower than in SWIFT J1753.5-0127. This gives a correspondingly more sensitive view of the UV and soft X-ray emission,

where it is clear that there is a large, cool disc seen in the UV and EUV bandpass (Esin et al. 2001; McClintock et al. 2001) which is completely inconsistent in luminosity and temperature with the much weaker, higher temperature 'disc' emission seen in soft X-rays (Frontera et al. 2001; 2003; Reis, Miller and Fabian 2009). There are plainly *two* components in this source, one which is consistent with a truncated disc, making no impact on the soft X-ray emission, *and* another component which produces weak soft X-ray flux. This is very similar to the spectrum of 24 as shown in Figure 3.11.

Thus for the late stage decline, our modelling with an irradiated disc is not supported by the data. The cross-correlation of the rapid variability clearly shows that the optical/UV cannot be made by reprocessing in the outer disc, while XTE J1118+480 clearly shows that the soft X-rays form a separate component to the observed UV/EUV emission from the (truncated!) disc. What then produces the observed optical/UV emission, and what produces the observed soft X-ray component ?

4.3 Optical/UV emission

As noted by Motch et al. (1985) in GX339-4, the X-ray emission in the dim low/hard state can extrapolate back quite accurately to fit the optical spectrum (see also Corbel and Fender 2002; Nowak 2005). One way to produce this is via a single synchrotron component from the innermost post-shock region of the jet. This is self absorbed in the IR, strongly suppressing the emission at lower frequencies. As the jet stretchs out , each part of it produces a synchrotron component which peaks at a lower frequency than those closer to the center. All of these make the flat spectrum seen in the radio (e.g. Markoff et al. 2005; Maitra et al. 2009). However, the non-thermal synchrotron makes the optical and X-ray emission from a single scattering in a single region, so it is hard to see how this can make the weak anticorrelation between the optical and X-ray flux with lead of a few

hundred milliseconds which seems typical of this state (Motch et al. 1985; Kanbach et al. 2001; Gandhi et al. 2008; Durant et al. 2008).

Conversely, the cross-correlation signal *can* be explained if the optical emission is from the jet, while the X-ray emission is from the corona (Malzac et al. 2004). However, the close match of the optical and X-ray spectra is then very unexpected if these are really from different components.

Instead, if the spectrum is formed from thermal Comptonisation from self-produced cylo-synchrotron photons in the hot flow then there can be complex time variability properties imprinted via propagating fluctuations through an inhomogeneous flow (Kotov et al. 2001; Arévalo and Uttley 2006). Whether these can indeed explain the anti-correlation between optical and X-ray by such spectral pivoting (Körding and Falcke 2004) remains to be seen.

4.4   Soft X-ray component

4.4.1   Continuum Curvature of the X-ray emission

If the spectrum is pivoting on short timescales then its time average cannot be described by a single thermal Comptonisation component and instead will be curved. This curvature would produce excess soft X-ray emission over that of the assumed single Comptonised continuum. Similar curvature can also be produced by including relativistic dynamics, as the electrons closest to the black hole are moving faster (Niedźwiecki 2005).

Excess continuum emission at soft X-rays can also be produced even in a single temperature Comptonised model. The multiple scatterings only merge into a power law if the

optical depth is close to unity, and even then the first few scatterings can be distinct if the seed photons are intrinsically anisotropic. This is always the case if the seed photons come from the disc, but the curvature is in the wrong sense (soft X-ray deficit with respect to harder X-rays) for a corona overlying the disc, where all the disc photons come from below (Haardt and Maraschi 1993). Instead, Comptonisation in a hot flow illuminated by a truncated disc has all the photons comming from the side, which may be able to cause curvature in the opposite sense, giving a small soft excess as required. However, this requires that the disc is the main source of seed photons and does not work if the self-produced cyclo-synchrotron photons are dominant as these should be isotropic.

While some continuum curvature seems inevitable, its effects should be strongest close to the seed photon energy. Since the optical does lie so convincingly on the extrapolated hard X-ray emission, it seems most likely that the seed photons are below the optical, making it hard to imagine that this can produce a noticeable effect on the X-ray spectrum.

4.4.2 Companion Star

Zurita et al. (2008) pointed out that a M-type companion star is needed to fit within the Roche lobe of a 3.24 hr orbit for SWIFT J1753.5-0127. Some M-type stars emit X-rays and their spectra are usually soft(extend down to less than 10 keV). However, the maximum X-ray luminosity is $\leq 10^{30}$ ergs s^{-1}, far below that required here.

4.4.3 Synchrotron Radiation from the jet

While there is no simultaneous radio data, a flat spectrum, steady radio jet is ubiquitously seen in the low/hard state with $L_R \propto L_X^{0.7}$ (see also Fender et al. 2009 for a review). We use this relation to scale the radio emission seen by Cadolle Bel et al. (2007) to the

factor 3 lower X-ray flux seen in the last stage decline assuming a spectral break from (photon index) $\Gamma = 1$ in the self absorbed regime to 2.1 in the optically thin regime. Thus the only free parameter is the break energy. We fit this to spectrum 24 (the last with a significant detection of disc), along with a thermal Comptonisation spectrum with seed photons in the IR so that this makes both the optical/UV and hard X-rays. This requires that the jet remains self absorbed up to soft X-ray energies. This is substantially higher than the IR break predicted in the models of Markoff et al. (2005).

4.4.4   Residual Inner Disc

Evaporation of the disc by thermal conduction is a plausible mechanism to form a truncated disc/ hot inner flow geometry (e.g. Liu et al. 1999). Counterintuitively, this is not most efficient at the smallest radii, as these also have the highest coronal densities, so have the highest condensation rates. Evaporation first erodes a *gap* in the disc, leaving a residual inner disc. This gap expands radially, eventually giving a fully truncated disc if the mass accretion rate is low enough(Mayer and Pringle 2007). However, close to the transition, the residual disc can remain. This geometry allows the outer disc to carry all the mass accretion rate. This disc evaporates into a corona, truncating it at some large radius into a coronal flow which carries all the mass accretion rate. However, as the flow accretes to smaller radii, the increasing density gives an increasing condensation rate and some small fraction of the material can condense out of the hot flow. This forms a cool ring at the innermost radii, with a mass accretion rate which is only a small fraction of the total mass accretion rate, with the rest of the material accreting via the coronal flow(Liu and Meyer-Hofmeister 2001).

Reprocessing is still an issue, but if the ring is small, extending over a very narrow range of radii, then it does not subtend a large solid angle to the coronal X-ray emission,

so could potentially produce the large observed ratio of coronal to (inner) disc luminosity.

4.4.5 Irradiation of the inner face of the inner disc

The temperature of the irradiated region is required to be substantially hotter than that of the disc itself, requiring a very small reprocessing area. This seems very unlikely for a central source illuminating a thin disc. However, the disc has some (small) half thickness, H_d, so its inner rim forms a distinct, small area $\approx 4\pi R_d H_d$ and subtends a solid angle $\approx H_d/R_d \times 4\pi$ to the central source. The small reprocessing area found in section 3.3.2 above corresponds to $H_d/R_d \sim 0.004$, predicting $f_{in} = (1-a)H_d/R_d \approx 0.002$, where a is the the reflection albedo. This is a factor 5 smaller than f_{in} derived from the data, but potentially feasible given the large uncertainties both on the parameters and on the modelling.

4.4.6 Ionized Reflection

Hiemstra et al. (2009) suggest that the weak soft X-rays are produced by a small amount of ionised reflection being present in the spectrum. However, if the disc really is recessed, the the solid angle subtended by it is small, in the same way that the effects of illumination should be small. However, the reflection could instead come from the *outer* disc. At first sight this seems unlikely as the outer disc is even further from the X-ray source, so less strongly illuminated and subtending an even smaller solid angle. However, grazing incidence angle illumination leads to an expanded outer disc atmosphere, subtending a solid angle of $\Omega/2\pi \sim 0.1 - 0.2$ as observed, covered by a thin, ionised skin (Jimenez-Garate et al. 2002). It remains to be seen whether such models can lead to enough soft X-ray reflection for the low mass accretion rates regimes here.

Chapter 5

Conclusion

The combined *Swift* and *RXTE* observations from the black hole transient SWIFT J1753.5-0127 give one of the best datasets to probe the evolution of the inner edge of the accretion disc in the low/hard state. These instruments cover the optical/UV and soft/hard X-ray bandpasses, giving a detailed picture of the spectral evolution during the low/hard state outburst.

We fit these with a sophisticated irradiated disc model and find that this gives a self-consistent picture around the outburst peak. Weak irradiation increases the inferred radius of the inner disc by a factor ~ 1.5. Photons from the disc are the seeds for Compton upscattering to produce the hard X-ray emission, and this hard X-ray emission weakly illuminates the outer disc to produce the observed optical/UV by reprocessing, as confirmed by the optical/X-ray cross-correlation (Hynes et al. 2009).

However, we find clear evidence that the model breaks down as the source flux declines. The optical spectra require increasingly unlikely levels of reprocessing to explain the observed emission. A change in origin of the optical emission is confirmed by the dramatic change in optical/X-ray cross-correlation signal (Hynes et al. 2009). While the cross-correlation can be explained in models where the optical is produced by the jet and the X-rays in a corona (Malzac et al. 2004), this does not explain the excellent match between the optical and X-ray spectra. Instead it seems more likely that there is a single component connecting the optical and X-ray spectra. The complex cross-correlation then remains an issue especially for a single synchrotron component from the jet, but it may potentially be explained by thermal Comptonisation of IR cyclo-synchrotron emission in

an inhomogeneous hot flow.

More fundamentally for the focus of this thesis, the soft X-ray emission during the decline may not be from the disc either. If it is, its radius does not change markedly from that seen at the outburst peak, in clear conflict with the predictions of the truncated disc model. But it also implies that the mass accreting through the disc is much less than the mass accretion rate required to power the corona. Yet it seems most likely that the mass does accrete through the outer disc, in which case the observed weak soft X-ray disc emission is a problem. Either the mass accretes through the disc but most of the energy is transported vertically *and* radially (to get around the reprocessing limits) by magnetic fields to power a small, central hard X-ray corona, or the soft X-rays are from an additional component, with the truncated disc peaking in the UV.

The lower absorption to XTE J1118+480 allows us to distinguish between these possibilities. Here, we can see a cool component peaking in the UV which is clearly distinct from the soft X-ray emission. The UV component fits well to a cool disc, truncated at large radii, so the soft X-ray component cannot be the same material. This may still be associated with the inner disc, perhaps from irradiation of its inner rim, or via a residual inner disc in the discontinuous disc geometry predicted by evaporation models (e.g. Liu and Meyer-Hofmeister 2001). However, it is also possible that the soft X-rays are instead produced in a completely different way, such as ionised reflection from grazing incidence angle illumination of the outer disc, or emission from the jet. Whatever their origin, it is clear from XTE J1118+480 that the weak soft X-ray component seen in the dim low/hard state does not trace the inner edge of the disc, so cannot be used to constrain the truncated disc models.

Bibliography

Arévalo P and Uttley P 2006 MNRAS **367**, 801–814.

Cabanac C, Fender R P, Dunn R J H and Körding E G 2009 MNRAS **396**, 1415–1440.

Cadolle Bel M, Ribó M, Rodriguez J, Chaty S, Corbel S, Goldwurm A, Frontera F, Farinelli R, D'Avanzo P, Tarana A, Ubertini P, Laurent P, Goldoni P and Mirabel I F 2007 ApJ **659**, 549–560.

Cadolle Bel M, Rodriguez J, Goldwurm A, Goldoni P, Laurent P, Ubertini P and Mereghetti S 2005 *The Astronomer's Telegram* **574**, 1–+.

Corbel S and Fender R P 2002 ApJ **573**, L35–L39.

di Matteo T, Celotti A and Fabian A C 1997 MNRAS **291**, 805–+.

Done C and Davis S W 2008 ApJ **683**, 389–399.

Done C and Gierliński M 2003 MNRAS **342**, 1041–1055.

Done C, Gierliński M and Kubota A 2007 A&A Rev. **15**, 1–66.

Dunn R J H, Fender R P, Körding E G, Cabanac C and Belloni T 2008 MNRAS **387**, 545–563.

Durant M, Gandhi P, Shahbaz T, Fabian A P, Miller J, Dhillon V S and Marsh T R 2008 ApJ **682**, L45–L48.

Esin A A, McClintock J E, Drake J J, Garcia M R, Haswell C A, Hynes R I and Muno M P 2001 ApJ **555**, 483–488.

Esin A A, McClintock J E and Narayan R 1997 ApJ **489**, 865–+.

Fabian A C, Iwasawa K, Reynolds C S and Young A J 2000 PASP **112**, 1145–1161.

Fender R, Garrington S and Muxlow T 2005 *The Astronomer's Telegram* **558**, 1–+.

Fender R P, Belloni T M and Gallo E 2004 MNRAS **355**, 1105–1118.

Fender R P, Homan J and Belloni T M 2009 MNRAS **396**, 1370–1382.

Frontera F, Amati L, Zdziarski A A, Belloni T, Del Sordo S, Masetti N, Orlandini M and Palazzi E 2003 ApJ **592**, 1110–1118.

Frontera F, Zdziarski A A, Amati L, Mikolajewska J, Belloni T, Del Sordo S, Haardt F, Kuulkers E, Masetti N, Orlandini M, Palazzi E, Parmar A N, Remillard R A, Santangelo A and Stella L 2001 ApJ **561**, 1006–1015.

Gallo E, Migliari S, Markoff S, Tomsick J A, Bailyn C D, Berta S, Fender R and Miller-Jones J C A 2007 ApJ **670**, 600–609.

Gandhi P, Makishima K, Durant M, Fabian A C, Dhillon V S, Marsh T R, Miller J M, Shahbaz T and Spruit H C 2008 MNRAS **390**, L29–L33.

Gierliński M, Done C and Page K 2008 MNRAS **388**, 753–760.

Haardt F and Maraschi L 1993 ApJ **413**, 507–517.

Hiemstra B, Soleri P, Méndez M, Belloni T, Mostafa R and Wijnands R 2009 MNRAS **394**, 2080–2088.

Hynes R I, Mauche C W, Haswell C A, Shrader C R, Cui W and Chaty S 2000 ApJ **539**, L37–L40.

Hynes R I, O'Brien K, Mullally F and Ashcraft T 2009 *ArXiv e-prints* .

Ingram A, Done C and Fragile P C 2009 MNRAS **397**, L101–L105.

Jimenez-Garate M A, Raymond J C and Liedahl D A 2002 ApJ **581**, 1297–1327.

Kanbach G, Straubmeier C, Spruit H C and Belloni T 2001 Nature **414**, 180–182.

Körding E and Falcke H 2004 A&A **414**, 795–806.

Kotov O, Churazov E and Gilfanov M 2001 MNRAS **327**, 799–807.

Krolik J H, Hawley J F and Hirose S 2005 ApJ **622**, 1008–1023.

Kubota A and Done C 2004 MNRAS **353**, 980–990.

Kubota A, Makishima K and Ebisawa K 2001 ApJ **560**, L147–L150.

Lasota J P 2001 *New Astronomy Review* **45**, 449–508.

Liu B F and Meyer-Hofmeister E 2001 A&A **372**, 386–390.

Liu B F, Yuan W, Meyer F, Meyer-Hofmeister E and Xie G Z 1999 ApJ **527**, L17–L20.

Maitra D, Markoff S, Brocksopp C, Noble M, Nowak M and Wilms J 2009 *ArXiv e-prints*
.

Makishima K, Takahashi H, Yamada S, Done C, Kubota A, Dotani T, Ebisawa K, Itoh
T, Kitamoto S, Negoro H, Ueda Y and Yamaoka K 2008 PASJ **60**, 585–.

Malzac J, Merloni A and Fabian A C 2004 MNRAS **351**, 253–264.

Markoff S, Falcke H and Fender R 2001 A&A **372**, L25–L28.

Markoff S, Nowak M A and Wilms J 2005 ApJ **635**, 1203–1216.

Matt G, Brandt W N and Fabian A C 1996 MNRAS **280**, 823–834.

Matt G, Fabian A C and Ross R R 1993 MNRAS **262**, 179–186.

Mayer M and Pringle J E 2007 MNRAS **376**, 435–456.

McClintock J E, Haswell C A, Garcia M R, Drake J J, Hynes R I, Marshall H L, Muno M P, Chaty S, Garnavich P M, Groot P J, Lewin W H G, Mauche C W, Miller J M, Pooley G G, Shrader C R and Vrtilek S D 2001 ApJ **555**, 477–482.

Miller J M, Homan J and Miniutti G 2006 ApJ **652**, L113–L116.

Miyamoto S, Kitamoto S, Hayashida K and Egoshi W 1995 ApJ **442**, L13–L16.

Morgan E, Swank J, Markwardt C and Gehrels N 2005 *The Astronomer's Telegram* **550**, 1–+.

Morris D C, Burrows D N, Racusin J, Roming P, Chester M, Verghetta R L, Markwardt C B and Barthelmy S D 2005 *The Astronomer's Telegram* **552**, 1–+.

Motch C, Ilovaisky S A, Chevalier C and Angebault P 1985 *Space Science Reviews* **40**, 219–224.

Narayan R and Yi I 1995 ApJ **452**, 710–+.

Niedźwiecki A 2005 MNRAS **356**, 913–924.

Nowak M 2005 Ap&SS **300**, 159–166.

Palmer D M, Barthelmey S D, Cummings J R, Gehrels N, Krimm H A, Markwardt C B, Sakamoto T and Tueller J 2005 *The Astronomer's Telegram* **546**, 1–+.

Poutanen J, Krolik J H and Ryde F 1997 MNRAS **292**, L21–L25.

Ramadevi M C and Seetha S 2007 MNRAS **378**, 182–188.

Reis R C, Fabian A C, Ross R R and Miller J M 2009 MNRAS **395**, 1257–1264.

Reis R C, Fabian A C, Ross R R, Miniutti G, Miller J M and Reynolds C 2008 MNRAS **387**, 1489–1498.

Reis R C, Miller J M and Fabian A C 2009 MNRAS **395**, L52–L56.

Ross R R and Fabian A C 1993 MNRAS **261**, 74–82.

Russell D M, Fender R P, Hynes R I, Brocksopp C, Homan J, Jonker P G and Buxton M M 2006 MNRAS **371**, 1334–1350.

Shakura N I and Sunyaev R A 1973 A&A **24**, 337–355.

Shapiro S L, Lightman A P and Eardley D M 1976 ApJ **204**, 187–199.

Smith D M, Heindl W A and Swank J H 2002 ApJ **569**, 362–380.

Still M, Roming P, Brocksopp C and Markwardt C B 2005 *The Astronomer's Telegram* **553**, 1–+.

Svensson R and Zdziarski A A 1994 ApJ **436**, 599–606.

van Paradijs J 1996 ApJ **464**, L139+.

Wardziński G and Zdziarski A A 2000 MNRAS **314**, 183–198.

Zhang G B, Qu J L, Zhang S, Zhang C M, Zhang F, Chen W, Song L M and Yang S P 2007 ApJ **659**, 1511–1518.

Zurita C, Durant M, Torres M A P, Shahbaz T, Casares J and Steeghs D 2008 ApJ **681**, 1458–1463.

Zycki P T, Done C and Smith D A 1999 MNRAS **305**, 231–240.